Seasonal and interannual variability of atmospheric ammonia over Guatemala driven by land use, biomass burning, and meteorological circulation

Christian Saravia[1], Pedro Saravia[2], and Katja Trachte[1]

[1]Department of Atmospheric Process, Brandenburg University of Technology (BTU) Cottbus-Senftenberg, Burger Chaussee 2, LG 4/3 Campus Nord, 03044, Cottbus, Germany
[2]Universidad de San Carlos de Guatemala, Escuela Regional de Ingeniería Sanitaria (ERIS), Ciudad Universitaria, 11° avenida Zona 12, Ciudad de Guatemala, Guatemala

Correspondence to: Christian Saravia (saravchr@b-tu.de)

Abstract.

Ammonia (NH_3) is a key atmospheric precursor of fine particulate matter and a marker of agricultural and biomass burning emissions. In Central America, NH_3 variability remains largely unquantified. This study presents the first integrated spatiotemporal assessment of atmospheric NH_3 over Guatemala (2015–2023) using multi-satellite observations (IASI A/B/C), combined with MODIS fire data, Sentinel-2 land cover, ERA5 meteorology, and CAMS reanalysis. Annual median NH_3 columns remained relatively stable, reflecting persistent agricultural sources dominated by fertilizer use and livestock. Significant anomalies occurred in 2016, 2020, and 2023, with 2020 showing the highest annual and monthly NH_3 levels. Seasonal peaks in April–May coincided with the regional fire season, followed by a sharp decline after rainfall onset. Hotspots were consistently detected in northern (Petén–Quiché) and southern (Escuintla) agricultural regions. The most extreme episode in April 2020 recorded 957 active fires over ~1,486 km^2, largely within the Maya Biosphere Reserve. Elevated temperature (+0.3 °C above the 2015–2023 mean) and high precipitation (+17% above average) favored NH_3 accumulation despite reduced anthropogenic activity during the COVID-19 lockdown. These results indicate that Guatemala's NH_3 variability is shaped by a stable agricultural baseline with superimposed fire-driven peaks, modulated by climatic anomalies. Continuous satellite monitoring is essential to improve emission inventories and support strategies to reduce biomass burning impacts across Central America.

1 Introduction

Atmospheric ammonia (NH_3) utilizes a considerable influence on air quality and ecological integrity through its potential for long-range transport and interaction with prevailing meteorological conditions (Zhou et al., 2019). As a reactive nitrogen (Nr) compound, NH_3 plays a fundamental role in the global nitrogen cycle and a variety of biogeochemical processes, representing a dominant form of nitrogen present in terrestrial and atmospheric systems (Sutton et al., 2007, 2013; Whitburn et al., 2016b). Despite its relatively short atmospheric lifetime ranging from several hours to a few days due to its high deposition efficiency

and conversion into particulate ammonium, current surface-based monitoring approaches remain inadequate for providing accurate global emission estimates, often introducing substantial uncertainties (Dammers et al., 2016; Herrera et al., 2022). NH_3 is also a key component in atmospheric chemistry and in the coupling of nitrogen and carbon cycles within ecosystems, with broad consequences regarding climate regulation, agricultural sustainability, air quality and public health. NH_3 emissions

35 originate from both natural and anthropogenic activities, with the latter contributing the majority of the global NH_3 burden. The agricultural sector remains the principal source, accounting for over 81% of total anthropogenic emissions globally (Van Damme et al., 2021; Wyer et al., 2022), while additional anthropogenic contributions stem from residential combustion, vehicular exhaust, industrial production, and wastewater treatment systems (Abeed et al., 2022; Dragosits et al., 2002; Sutton et al., 2007).

40

Although agriculture particularly through the use of fertilizers and manure remains the dominant source of atmospheric NH_3, recent studies suggest that emissions from non-agricultural sources, particularly those associated with vehicular traffic, may be significantly underestimated (Chen et al., 2024; Chen and Wang, 2025; Farren et al., 2020; Gu et al., 2023; Zhou et al., 2017). Empirical evidence indicates that diesel vehicles equipped with selective catalytic reduction (SCR) systems can emit

45 NH_3 as an unintended byproduct (Sun et al., 2017; Wen et al., 2023). Vehicular NH_3 emissions are known to contribute to the rapid formation of fine particulate matter, particularly during air pollution episodes, underscoring the predominant role of fossil fuel combustion as a non-agricultural NH_3 source in urban environments (Farren et al., 2020, 2021; Pan et al., 2016). Additionally, various industrial activities including steel production (Chen and Wang, 2025), power generation, and fertilizer manufacturing also release substantial amounts of NH_3 into the atmosphere (Van Damme et al., 2018; Gu et al., 2023).

50

In recent decades, satellite remote sensing has significantly advanced the detection of atmospheric NH_3, leading to the development of several global NH_3 emission datasets, notably from the Infrared Atmospheric Sounding Interferometers (IASI) instrument. For this study, we also include fire-based emission datasets such as the Global Fire Emissions Database (Giglio et al., 2006, 2013; van der Werf et al., 2010, 2017), the Global Fire Assimilation System (Remy and Kaiser, 2014) developed by

55 the European Centre for Medium-Range Weather Forecasts (ECMWF), and two fire products from the National Aeronautics and Space Administration (NASA), based on fire radiative power (FRP) measurements (Fu et al., 2020; Li et al., 2020; Remy and Kaiser, 2014; Vermote et al., 2009; Wooster et al., 2003).

Central America's climate is significantly shaped by the two oceans it borders, with the vast Pacific Ocean, spanning nearly

60 half the Earth's circumference at the equator, being especially crucial for climate regulation by El Niño brings drier conditions to Guatemala, while La Niña produces more precipitation (Bardales Espinoza et al., 2019) Guatemala's geomorphological attributes and geospatial coordinates inherently facilitate a multitude of microclimatic zones and pronounced climatic heterogeneity, the variability has been amplified in recent years by the nation's persistent susceptibility to extreme meteorological phenomena, including prolonged arid periods and intense tropical cyclones, both of which are intensified by

65 the overarching impacts of anthropogenic climate change (Alfaro Marroquín and Gómez, 2019). Guatemala's climate deviates from the typical four-season delineation observed in the Northern Hemisphere. Instead, it is characterized by two distinct periods: the wet season, spanning from May to October, and the dry season, occurring from November to April (INSIVUMEH, 2018; Orrego León et al., 2021).

70 Furthermore, these climate condition directly influence and intensify of biomass burning events, particularly during dry season, Guatemala is exposed to a variety of threats, with wild-fires being one of the main threats in recent decades (CONRED, 2025). Guatemala has experienced increasing concern from fire-related activities that are strongly tied to agricultural expansion, shifting cultivation, and deforestation. These practices, often used to clear land for crops or grazing, are typically intensified during the dry months, aligning with peak fire activity (Liu et al., 2024; Monzón-Alvarado et al., 2012). Guatemala consistently

75 reports a high number of fire hotspots (CONRED, 2025), especially in years dominated by El Niño-induced drought conditions (Chuvieco et al., 2019; CONRED, 2025; Giglio et al., 2013). The recurrence of such fires in forested and agro-pastoral zones not only transforms land cover but also releases large quantities of reactive trace gases and aerosols, including atmospheric NH_3 into the atmosphere (Andreae, 2019; Pohl et al., 2022; Wyer et al., 2022). Despite this, the role of biomass burning as a driver of NH_3 emissions remains underexamined in Central American air quality studies.

80

Despite the increasing availability of satellite-based datasets for monitoring atmospheric NH_3 there remains a significant lack of regional-scale studies in Central America, particularly in Guatemala, where land use dynamics and biomass burning are likely to contribute substantially to NH_3 emissions. Previous research has often overlooked the integrated role of multiple environmental drivers such as meteorological variability, and land cover change. This study investigates the monthly

85 spatiotemporal dynamics of atmospheric NH_3 emissions in Guatemala from 2015 to 2023, using three satellite observations from IASI onboard of the Meteorological Operational satellite programme (MetOp), MetOp-A, MetOp-B, and MetOp-C, in combination with land cover classification from the Environmental Systems Research Institute (ESRI), ERA5 meteorological data, and fire activity from MODIS. The research aims to identify hotspots and the interannual and seasonal NH_3 emission variability. In addition, this study employed spatial clustering using k-means algorithm to partition NH_3 emission patterns and

90 explore their heterogeneity, with a particular focus on land cover types and the influence of fire-pixel activity. To ensure the reliability of the fire data, fire-pixels from MODIS with a confidence level >70% were included in the analysis. A case study in 2020 further examines peak emission conditions in relation to extreme fire events linked to agriculture and meteorological anomalies. The result of this study provides critical insight for a region where such integrated analyses remain scarce.

2 Methodology

2.1 Data analysis

This section presents a comprehensive analysis of atmospheric ammonia (NH_3) concentrations and related environmental factors in Guatemala from 2015 to 2023, utilizing concatenated IASI A/B/C sensor data, incorporating both morning and night observations for enhanced representativeness. We first detail the spatiotemporal variability of NH_3 emissions, examining annual trends that reveal generally the baseline with notable outliers and a potential recent increase. Seasonal patterns are also explored, highlighting a distinct annual cycle with a pronounced peak during the months of April and May. Spatially, elevated NH_3 emissions are consistently observed in the northern and southern regions where cropland is dominated, contrasting with lower rates in the central midlands, a pattern further elucidated by k-means cluster analysis which categorizes regions by emission intensity. Utilizing these IASI observations, specific NH_3 source regions within Guatemala have been identified and characterized, revealing that the majority of these elevated emission zones are primarily associated with agricultural practices (e.g., farming and spreading activities) and, in some northern areas, a combination of rangeland and built-up development.

Subsequently, the interrelationships between NH_3, other air pollutants (nitrogen dioxide [NO_2] and sulfur dioxide [SO2]), fire activity, and key meteorological variables (temperature, relative humidity, boundary layer height, surface pressure, and total precipitation) are explored through Pearson correlation analysis. This investigation reveals significant associations, such as strong positive correlations between NH_3 and both NO_2 and fire activity, alongside inverse relationships with parameters like relative humidity. Finally, a case study of the April 2020 NH_3 anomaly is presented. This period is particularly noteworthy for recording the highest emission levels during the study, coinciding with specific meteorological conditions, fire activity, and the COVID-19 lockdown period. This detailed examination integrates spatial distribution maps, wind patterns, and vertical profiles to provide deeper insights into the potential drivers and atmospheric dynamics contributing to this significant NH_3 event.

2.2 Study location

This study focuses on the Republic of Guatemala, a Central American country situated between latitudes 13.5°N to 17.8°N and longitudes 88.2°W to 92.2°W. Guatemala encompasses a diverse range of ecological regions, topographical variations, and land use patterns, all of which have significant implications for atmospheric NH_3 dynamics. The country is characterized by a complex zone of agricultural lands, forested highlands, volcanic zones, and rapidly urbanizing areas factors that contribute to both natural and anthropogenic NH_3 emissions. Agriculture remains a cornerstone of the Guatemalan economy and landscape, with extensive cultivation of crops such as maize, bean, coffee, sugarcane, oil palm, and bananas (FAO, 2019; Hervas, 2019; Lopez-Ridaura et al., 2019). Fertilizer application and livestock farming are particularly prevalent in rural regions, making the agricultural sector a dominant source of NH_3 emissions nationwide. Meanwhile, increasing urbanization

and industrialization, especially around Guatemala City and its metropolitan zone, have introduced additional non-agricultural emission sources, such as vehicular exhaust, industrial activity, and waste treatment processes. Moreover, Guatemala experiences a pronounced dry season (typically November to April) and rainy season (May to October) (Alfaro Marroquín and Gómez, 2019; Bardales Espinoza et al., 2019; INSIVUMEH, 2018; Orrego León et al., 2021), which strongly modulate fire

130 activity, atmospheric transport conditions, and deposition processes relevant to NH₃ dispersion. Frequent wildfires, especially in the Petén department (northern area of Guatemala) and central highlands during the dry season, contribute further to the atmospheric burden of reactive nitrogen species. The height of Guatemala varies from sea level to 3,000 m above sea level (a.s.l) in the central plateau and with volcanic peaks that reach 4,200 m a.s.l. (IGM, 2002). Figure 1 shows the digital elevation model (DEM) of the topographic surface in meter over Guatemala using the European Space Agency, 2024). These topographic

135 elevation and environmental anthropogenic conditions make Guatemala an important, yet understudied, region for evaluating NH₃ variability and its interaction with land cover, climate, and pollution.
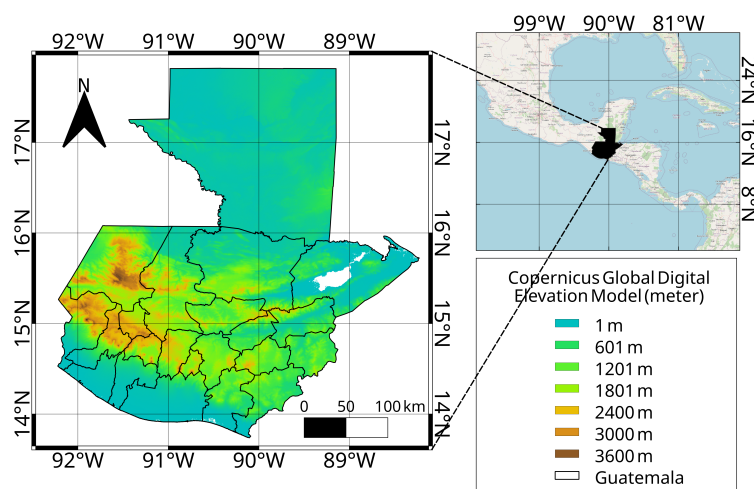
Figure 1: Guatemala elevation (m) from Copernicus Global Digital Elevation Model.

140

2.3 ESRI land cover class map

The ESRI Land Use Land Cover (LULC) 2020 dataset was released in June 2021 by the Environmental Systems Research Institute (ESRI) was developed using deep learning models trained on more than 5 billion manually labeled pixel samples derived from Sentinel-2 satellite imagery (Karra et al., 2021). According to (ESRI, 2021) these training samples were collected

145 from 24,000 image tiles globally, each measuring 510 × 510 pixels, and reflect a wide range of land surface types. The LULC 2020-ESRI dataset, based on data from the European Space Agency's Sentinel 2 mission with 10 m spatial resolution, enables

land cover mapping at both national and local scales. The LULC 2020 map is classified into nine classes: Water, Trees, Flooded vegetation, Crops, Built area, Bare ground, Snow/Ice, Clouds, and Rangeland (Karra et al., 2021).

2.4 Ammonia (NH₃) observation from IASI

150 Atmospheric total column measurements of NH_3 were obtained from the Infrared Atmospheric Sounding Interferometer (IASI), an instrument onboard of the MetOp A/B/C satellites launched in 2006, 2012, and 2018, respectively (Clarisse et al., 2009, 2019; Coheur et al., 2009). IASI works with a cross-track scanning swath approximately 2200 km wide and provides measurements with a nadir pixel diameter of about 12 km. Positioned aboard sun-synchronous polar-orbiting satellites, the instrument enables near-global coverage twice daily during both daytime and nighttime corresponding to local solar overpass

155 times of approximately 09:30 and 21:30, respectively (Clarisse et al., 2010; Van Damme et al., 2017; Whitburn et al., 2017). The vertical sensitivity of NH_3 retrievals is primarily concentrated within the boundary layer, where atmospheric ammonia is most abundant, and is strongly modulated by the thermal difference between the Earth's surface and the overlying atmospheric layers (Clarisse et al., 2009; Whitburn et al., 2016a).

160 This study employed version 4 of the ANNI-NH_3 retrieval product (Clarisse et al., 2023), derived from IASI Metop-A/B/C morning and night overpasses for the period 2015–2023, and regridded to a 0.25° × 0.25° spatial resolution. A major enhancement in this version is the incorporation of the vertical column averaging kernel (AK), which is essential for aligning satellite retrievals with chemistry-transport model simulations by mitigating the influence of the priori NH_3 vertical profiles applied during retrieval. While spatial patterns remain consistent with previous versions, total column values are approximately

165 15–20% higher due to improvements in the high-resolution infrared retrieval configuration (HRI), version 4 offers improved uncertainty characterization and enhanced temporal uniformity of the dataset from 2007 to 2023 (Clarisse et al., 2023). The retrieval algorithm estimates a hyperspectral range index from IASI spectra and converts it into NH_3 total column densities using an artificial neural network (Van Damme et al., 2021; Franco et al., 2018; Whitburn et al., 2017).

170 This process is supported by consistent ERA5 meteorological reanalysis data, making the product suitable for assessing interannual variability and long-term trends (Hersbach et al., 2020). The instrument's detection limit, which depends on atmospheric conditions such as thermal contrast and NH_3 abundance, is estimated to be as low as $4–6 × 10^{15}$ molecules cm^{-2} (Clarisse et al., 2009). The ANNI- NH_3 product has been validated against in situ observations, showing strong regional correlations (Van Damme et al., 2021, 2022; Guo et al., 2012), and has been widely applied in both global (Evangeliou et al.,

175 2021) and regional NH_3 emission studies (Chen et al., 2023; Marais et al., 2021a, b).

The NH_3 vertical profiles were obtained from the ECMWF, Atmospheric Composition Reanalysis 4 (EAC4), produced by the Copernicus Atmosphere Monitoring Service (CAMS). The vertical resolution of NH_3 in the model is defined by 60 hybrid sigma-pressure levels, which provide a detailed representation of the atmospheric structure, particularly near the surface where

180   most emissions occur (Inness et al., 2019). These reanalysis datasets incorporate satellite observations and model simulations
       to provide globally consistent, spatially and temporally resolved atmospheric composition data (Flemming et al., 2017; Inness
       et al., 2019).

       To identify spatial patterns in atmospheric NH₃ emissions and associated land cover characteristics, an unsupervised clustering
185   approach was applied. Clustering is a type of unsupervised machine learning that groups large datasets based on their similarity,
       allowing for more manageable and interpretable analyses (Ahmad and Dey, 2007; Pham et al., 2005). This analytical approach
       is particularly beneficial when there is limited or no prior knowledge about the underlying structure of the data (Gašparović et
       al., 2019). Among clustering methods, the k-means algorithm is one of the most commonly applied and reliable techniques. It
       partitions data into a predefined number of k clusters by iteratively determining central points, or centroids, for each group
190   (Pham et al., 2005). The algorithm requires the number of clusters to be specified in advance (Ahmad and Dey, 2007; Mahata
       et al., 2020). K-means operates using the squared Euclidean distance as its primary metric (Spencer, 2013), which quantifies
       the separation between two points within a Euclidean space of any dimension (Li et al., 2022). The Euclidean distance between
       two points, p and q, in a j-dimensional space is mathematically expressed as $d(p,q)$.

195
$$d(p,q)\sqrt{(p_1-q_1)^2+(p_1-q_1)^2+\ldots+(p_j-q_j)^2} \tag{1}$$

       The k-means algorithm divides a dataset into k clusters by aiming to minimize the variance within each group (Li et al., 2022).
       It operates on a set of input samples $X=\{x^1,\ldots,x^n\}$, where each $X^m=\{x_1^m, x_2^m,\ldots,x_j^m\}$ represents an observation composed
       of j variables, and $m \in X=\{1,\ldots,n\}$, with n being the total number of observations. These samples are categorized into k
200   clusters $(S_1, S_2, \ldots S_k)$ with the goal of minimizing the total intra-cluster variance $(S_{i=1,\ldots,k})$, as described in Equation (2):

$$\underset{S}{argmin} \sum_{i=1}^{k} \sum_{X \in S_i} \|X-\mu_i\|^2 \tag{2}$$

       The notation $\|X-\mu_i\|$ represents the squared Euclidean distance between each data point (X) and its assigned cluster centroid
205   μ_i within a multidimensional Euclidean space (Li et al., 2022). In this research, k-means clustering was utilized to examine
       the spatiotemporal patterns of NH₃ emissions throughout the specified timeframe (Anne Fouilloux, 2018; Pedregosa et al.,
       2011). To determine the most suitable number of clusters (k), the elbow method was employed (Umargono et al., 2019). This
       approach assesses the Cluster Sum of Squares (CSS) to identify the point at which the inclusion of additional clusters no longer
       significantly improves the model performance.

2.5 Meteorological data from ERA-5

Meteorological variables used in this study were obtained from the fifth-generation global reanalysis (ERA5) (Soci et al., 2024) dataset provided by ECMWF, (Hersbach et al., 2020). Originally available at a horizontal resolution of approximately 31 km, the data were resampled to a $0.25° \times 0.25°$ grid and both spatially and temporally interpolated to match the IASI NH_3 observation times and locations. The selected meteorological parameters include 2 m air temperature (t2m), 10 m wind speed (ws), boundary layer height (blh), relative humidity (derived using 2 m air temperature and dew point temperature), surface pressure (sp), and total precipitation (tp). Correlation analyses between these variables and atmospheric NH_3 concentrations were performed to better understand the meteorological drivers influencing NH_3 variability across Guatemala.

2.6 Fires and burned areas

Detected active fires for this work were sourced from the MODIS-Aqua/Terra Thermal Anomalies/Fire locations at 1 km FIRMS Near Real-Time (NRT) - Collection 6.1 (Giglio et al., 2021a). This product is processed by NASA's Land, Atmosphere Near real-time Capability for EOS (LANCE) Fire Information for Resource Management System (FIRMS), utilizing swath products (MOD14/MYD14). The thermal anomalies, or active fires, pinpoint the center of a 1 km pixel identified by the MODIS MOD14/MYD14 Fire and Thermal Anomalies algorithm (Giglio et al., 2003, 2006; Justice et al., 2010) as containing one or more fires within that pixel. While monitored at a 1×1 km^2 resolution, the system is capable of detecting fires as small as 100 m^2. Furthermore, MODIS captures data by scanning across the Earth's surface about every 1.48 seconds (Giglio et al., 2016).

This scanning mechanism produces 10 image lines in the along-track dimension, with each line capturing 1354 pixels in the along-scan dimension (Wolfe et al., 2002). For every detected fire pixel in this product, three key pieces of information are provided: fire location, fire detection confidence, and Fire Radiative Power (FRP) (Giglio et al., 2013). The fire location is defined by the central longitude and latitude of the pixel. Fire detection confidence assesses the probability of a pixel genuinely containing a fire and is categorized as low level: 0% to < 30%, nominal level: 30% to < 80%, high level: 80% to 100% (Giglio et al., 2016, 2021b, a; Hantson et al., 2013). However, several studies recommended using MODIS fire for nominal–high confidence to reduce the number of false alarms (Giglio et al., 2021b, a). Therefore, the study used fire detections with a nominal confidence level i.e., >70%. In addition, FRP, which quantifies the energy release rate from the fire (Wooster et al., 2003), was used as a filtering criterion to highlight the most significant fire hotspots. Only pixels with FRP values greater than 40 MW were considered in the analysis, ensuring that the dataset emphasized large and energetically relevant fire events rather than for a smalls cale or low intensity detections. FRP, which quantifies the energy release rate from the fire, according to the methodology proposed by (Wooster et al., 2003):

$$FRP = \frac{\sigma \times A_{pixel}}{\alpha \times \tau_4} (L_4 - L_{4b}) \text{ (Megawatt: MW)} \qquad (2)$$

A_{pixel} is the fire pixel area $\sigma = 5.6704 \times 10^{-8}\ Wm^{-2}\ K^{-4}$ is the Stefan–Boltzmann constant, $\alpha = 3.0 \times 10^{-9}\ Wm^{-2}\ sr^{-1}m^{-1}k^{-4}$ is the MODIS empirical constant, τ_4 is the atmospheric transmittance at 4 µm, and $L_4 - L_{4b}$ are radiances at 4

245 µm of the fire and background pixels (Wooster et al., 2003).

The burned analysis for this work was obtained by the Terra and Aqua combined MCD64A1 Version 6.1, a monthly global dataset gridded at 500 m that provides per-pixel burned-area and quality information (Giglio et al., 2018). The MCD64A1 mapping approach fuses 500 m Moderate Resolution Imaging Spectroradiometer (MODIS) surface reflectance imagery with

250 1 km MODIS active fire observations (Giglio et al., 2003, 2021b). The underlying algorithm uses a burn-sensitive Vegetation Index (VI) to create dynamic thresholds for composite data, the VI is calculated from MODIS shortwave infrared atmospherically corrected surface reflectance (bands 5 and 7) along with a measure of temporal texture (Giglio et al., 2006, 2018). The algorithm identifies and encodes the burn date for each 500-meter grid cell within individual MODIS tiles as the ordinal day of the calendar year and unburned land pixels, missing data, and water grid cells are assigned unique values (Giglio

255 et al., 2016). In addition to the burn date, the MCD64A1 product also provides data layers for Burn Data Uncertainty, Quality Assurance, and the First and Last Day of reliable change detection for the year (Dong et al., 2013; Freeborn et al., 2011; Giglio et al., 2003, 2021b; Justice et al., 2010).

3 Results

3.1 Spatiotemporal variability of NH₃

260 Fig. 2 shows the spatio-temporal variability of annual mean atmospheric NH_3 concentrations over Guatemala from 2015 to 2023, based on concatenated data from the IASI A/B/C sensors. The respective boxplots reveal a generally stable NH_3 concentration throughout the study period. However, the annual mean NH_3 concentrations varied, reaching a minimum of 4.12 $\times 10^{15}$ molecules/cm^2 $\pm$ 5.34 $\times 10^{14}$ molecules/cm^2 in 2018 and a maximum of 6.67 $\times 10^{15}$ molecules/cm^2 $\pm$ 5.62 $\times 10^{15}$ molecules/cm^2 in 2020. The highest annual amounts were observed in 2016 (5.46 $\times 10^{15}$ molecules/cm^2), 2020 (6.67 $\times 10^{15}$

265 molecules/cm^2), and 2023 (5.60 $\times 10^{15}$ molecules/cm^2), with values fluctuating around a consistent central tendency of 4.97 $\times 10^{15}$ molecules/cm^2 (Table S1). Furthermore, the analysis identifies some notable outliers, particularly in the year 2020, which recorded the highest concentration of 2.34 $\times 10^{16}$ molecules/cm^2, followed by 2016 (1.53 $\times 10^{16}$ molecules/cm^2), and 2023 (9.74 $\times 10^{15}$ molecules/cm^2), indicating substantial variability and peak emissions. The median NH_3 column densities remained relatively consistent throughout the years. The interquartile range (IQR), representing the spread of the central 50% of the data,

270 also shows limited variability indicating a degree of stability in NH_3 emission levels. Standard deviations are typically below 1.00 $\times 10^{15}$ molecules/cm^2, which further reinforce the low interannual variability.

The concatenated data from IASI A/B/C data of spatial distribution of annual mean of NH$_3$ emissions across Guatemala from 2015 to 2023 exhibited a consistent pattern of elevated emissions in the northern and southern regions. A consistent spatial

275   pattern of elevated NH$_3$ concentrations was observed, with discernible hotspots in the northern, north-central, and southern regions of the country. Conversely, the central midlands and highlands consistently displayed lower emission rates throughout the period. Annual mean concentrations varied significantly, with the highest values detected in 2020 and 2016. Specifically, the maximum value was observed in 2020, followed by 2016 and 2023. Despite these variations in overall annual mean concentrations, the spatial pattern of the hotspots remained consistent throughout the years. For instance, even during a year

280   with a lower overall annual mean like 2018, increased hotspot values were still evident in the southern region of Guatemala.
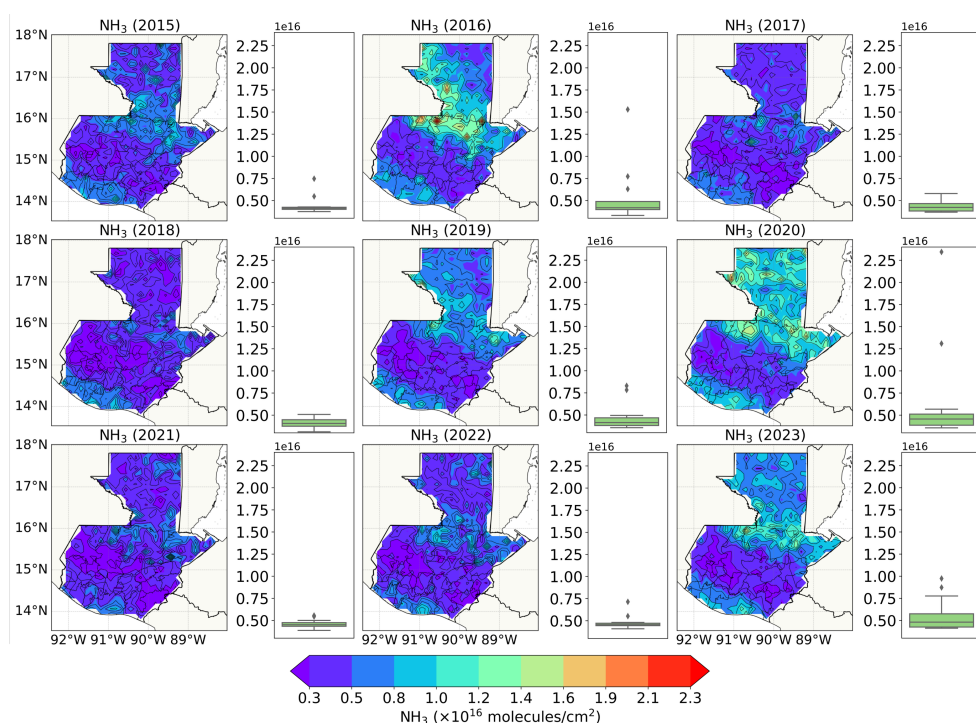
Figure 2: Annual means area-wide and boxplot of NH$_3$ emission ($\times 10^{16}$ molecules/cm^2) over Guatemala (2015–2023) from IASI A, B and C.

285

The mean monthly variation in atmospheric NH$_3$ emission over Guatemala reveals a distinct intra-annual pattern (Fig. 3). The analysis reveals a distinct pattern in NH$_3$ emissions with levels remaining relatively low and stable from January to March (Table S2) with monthly mean concentrations ranging from 3.59×10^{15} molecules/cm$^2 \pm 1.7 \times 10^{15}$ molecules/cm^2 (February) to 4.21×10^{15} molecules/cm$^2 \pm 2.04 \times 10^{15}$ molecules/cm^2 (January). A substantial increase in NH$_3$ is observed at the beginning

290   of April, with monthly mean values of 1.01×10^{16} molecules/cm$^2 \pm 4.43 \times 10^{15}$ molecules/cm^2 and in May with values of 9.80×10^{15} molecules/cm$^2 \pm 4.49 \times 10^{15}$ molecules/cm^2. These months also show the highest values in April reaching 2.33×10^{16}

molecules/cm^2 and May peaking at 2.72×10^{16} molecules/cm^2 respectively, indicating both significantly higher average emissions and larger variability. Emissions then exhibit a sharp decline from June onwards, with the monthly mean dropping to 5.77×10^{15} molecules/cm^2, returning to consistently stable concentrations by July (3.81×10^{15} molecules/cm^2) and remaining low through December, with monthly means hovering around 4.0×10^{15} molecules/cm^2. Sporadic outliers, representing instances of unusually high NH$_3$ emissions, are observed primarily during the April–May, corresponding to the months with the highest recorded maximum values.

The corresponding spatial distribution of monthly mean NH$_3$ emissions also displays the distinct seasonal pattern in concentration over Guatemala. From January to March, NH$_3$ concentrations are generally low across the country, with limited areas exhibiting elevated values. A substantial increase in both the magnitude and spatial coverage of NH$_3$ emissions is observed in April, with widespread elevated concentrations particularly in the northern and southern coastal regions, consistent with the highest monthly mean. This peak in emission intensity continues into May, maintaining high concentrations in these areas, aligning with its monthly mean located in northern and southern regions. Subsequently, a sharp decline in NH$_3$ concentrations is evident from June onwards, returning to consistently low levels by July and remaining stable through December. During these low-emission months, the spatial distribution of NH$_3$ is characterized by few hot-spots but and generally uniform low concentrations across the central midlands and highlands. This pronounced seasonality in spatial patterns aligns with the temporal variations observed in the overall time series.
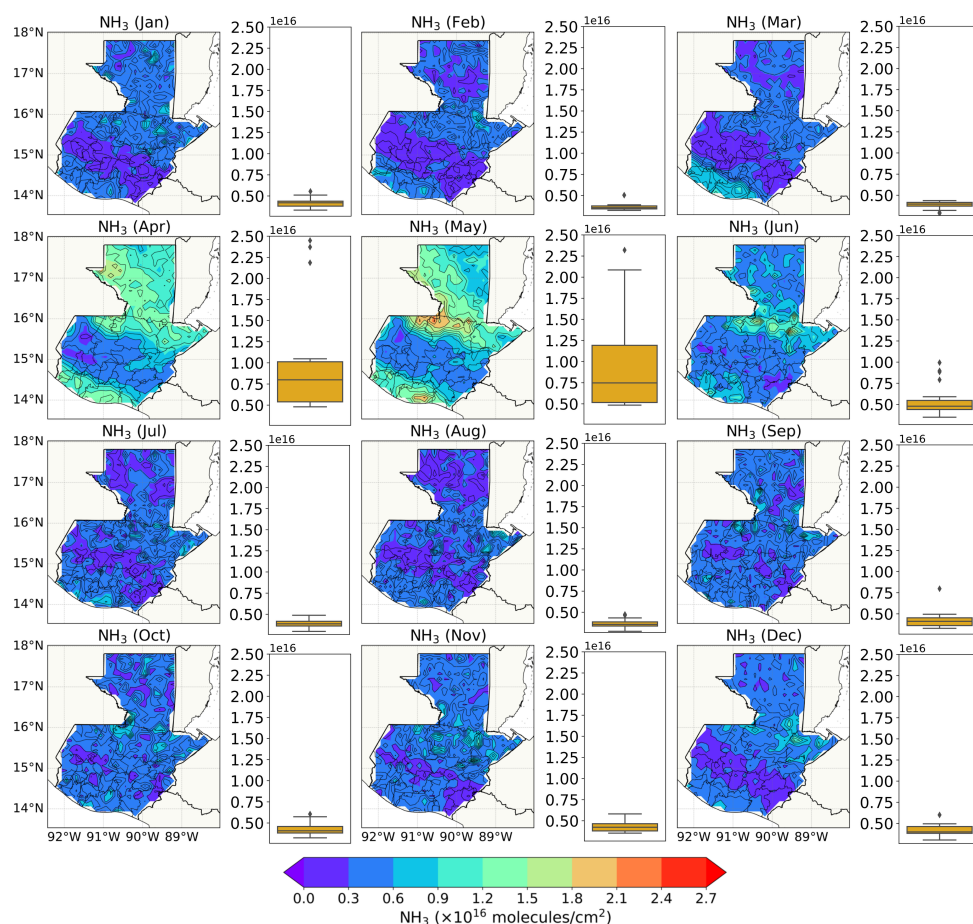
Figure 3: Monthly means area-wide and boxplot of NH$_3$ emission ($\times 10^{16}$ molecules/cm^2) over Guatemala (2015–2023) from IASI A, B and C.

3.2 Land cover classification driven a k-means clustering of NH$_3$ emissions

The spatial distribution of NH$_3$ emissions in Guatemala, based on the overall annual mean for the period 2015–2023, reveals six distinct hotspots (Fig. 4a). One of these high-emission areas is located in the southern region of the country in the department of Escuintla, while the remaining five are concentrated in the northern region. Among them, the most prominent hotspot is Area 4, situated within the departments of Alta Verapaz, Petén and Quiché, which exhibits the highest annual mean NH$_3$ values during the study period.

The k-means clustering partitions the country into three emission zones (Fig. 4b), each with distinct land cover profiles when integrated with ESRI data (Fig. 4c). Cluster 1 (red) associated to the highest NH$_3$ concentrations, is located in the northern, central-north, and southern regions and is dominated by cropland (16.7%; 4710.8 km^2) and rangeland (24.5%; 6934.2 km^2).

Tree cover remains extensive (53.2%; 15,024.6 km^2), while built-up areas are limited (3.4%; 948.6 km^2) as shown in Fig. 4d.
325   This composition reflects the strong role of intensive agricultural activity, particularly fertilizer use and livestock, in driving
the elevated emissions observed in this cluster. The complete land cover distribution across clusters is provided in Table 1.

Cluster 2 (yellow) represents moderate emission zones forming a transition around Cluster 1 and extending into northern,
eastern, and southwestern Guatemala (Fig. 4e). It is dominated by tree cover (58.9%; 26,891.6 km^2) and rangeland (30.3%;
330   13,844.6 km^2), with a comparatively small share of cropland (6.0%; 2724.7 km^2). Built-up areas account for 2.8% (1261.8
km^2), slightly larger in absolute terms than in Cluster 1. This land covers mix of forests, shrublands, and transitional agricultural
areas reflect semi-natural landscapes under moderate anthropogenic influence.

Cluster 3 (green), associated with the lowest NH$_3$ concentrations, covers the central, southern, and western regions. It is
335   characterized by high rangeland cover (34.3%; 11,893.3 km^2) and substantial tree cover (47.1%; 16,298.9 km^2), while cropland
is minimal (3.1%; 1088.6 km^2) (Fig. 4f). Notably, built-up areas occupy the largest proportion across clusters (14.8%; 5137.1
km^2), despite Cluster 3 having the smallest territorial extent. The coexistence of dense vegetation, moderate agricultural
activity, and significant urban development suggests a complex anthropogenic footprint, though with lower NH$_3$ emissions
than in Cluster 1.
340

Overall, Cluster 1 covers the smallest area (28,253.9 km^2) compared to Cluster 2 (45,662.3 km^2) and Cluster 3 (34,640.0 km^2),
yet it exhibits the highest NH$_3$ emissions. This elevated level is strongly associated with its land cover composition, particularly
the concentration of cropland and rangeland.

345   **Table 1: Land cover composition of percentage and area for the different cluster in Guatemala.**

LCC	Cluster 1		Cluster 2		Cluster 3	
	Percentage %	Area km^2	Percentage %	Area km^2	Percentage %	Area km^2
Water	1.94	548.97	1.78	812.44	0.64	221.61
Trees	53.16	15,024.57	58.89	26,891.61	47.05	16,298.85
Flooded Veg.	0.31	86.77	0.28	127.16	0	0.63
Crops	16.67	4710.8	5.97	2724.67	3.14	1088.56
Built Areas	3.36	948.62	2.76	1261.81	14.83	5137.06
Rangeland	24.53	6934.19	30.32	13,844.63	34.33	11,893.31
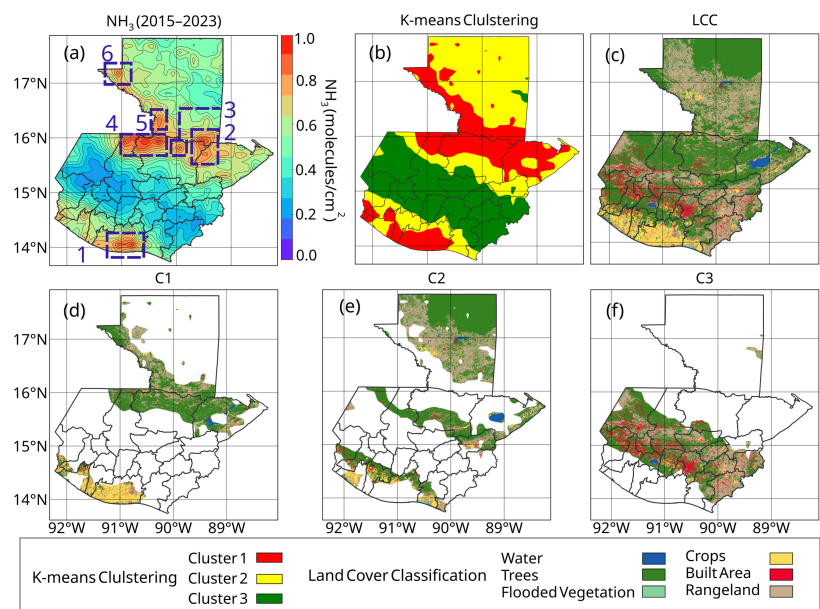
Figure 4: (a) Total column concentrations of NH₃ (2015–2023), (b) k-means cluster analysis with Cluster 1 (red color), Cluster 2 (yellow color) and Cluster 3 (green color). (c) ESRI Land Use/Land Cover across Guatemala, categorized into three clusters based on k-means combined with land cover types: water, trees, flooded vegetation, crops, built area, and rangeland, (d) C1 related to cluster 1, (e) C2 to cluster 2, and (f) C3 to cluster 3.

3.3 Fires

In order to connect the previously described ammonium patterns Fig. 5 shows the annual distribution of fires in Guatemala during the study period. The data reveal considerable interannual variability observed in both the number and distribution of fires, with mean monthly fire counts ranging from a minimum of 73 in 2022 to a maximum of 162 in 2016 (Table S3). During 2015, the mean monthly number of fires was 137, with a monthly maximum of 817 fires. Fire activity peaked in 2016 with the highest mean monthly count (162), followed by 2017 with 149. Notably, 2017 also recorded the highest monthly peak of 947 fires, indicating both more frequent and more intense fire events compared with the surrounding years.

In 2018, fire activity decreased sharply, with the mean monthly count dropping to 77 and the maximum monthly count to 383. The activity increased in 2019 (mean 133) and remained elevated in 2020 (mean 142), when the highest single month value of the entire study period was observed (957), coinciding with the COVID-19 pandemic. From 2021 onward, the number of fires generally shows a decreasing trend, with mean monthly counts dropping to 82 in 2021 and reaching its minimum of 73 in 2022 (maximum 247). Although 2023 showed a partial increase with mean of 119 and maximum 564, (with a maximum of 564), fire activity did not return to higher levels recorded from 2015-2020 period.

The spatial distribution of Fire Radiative Power (FRP) across Guatemala from 2015 to 2023 complements the annual fire
370   counts, showing both significant interannual variability and spatial heterogeneity in fire activity. Years with elevated fire
frequencies, such as 2017, 2019, 2020 and 2023, were also marked by widespread areas of moderate to high FRP, with hotspots
concentrated in the northern and southern regions. In contrast, years of reduced fire counts, including 2018, 2021 and 2022,
coincided with lower FRP intensity and a more limited spatial extent. These consistent patterns indicate fluctuating fire
regimen, where periods of intense and widespread fire activity alternated with years of reduced activity.

375
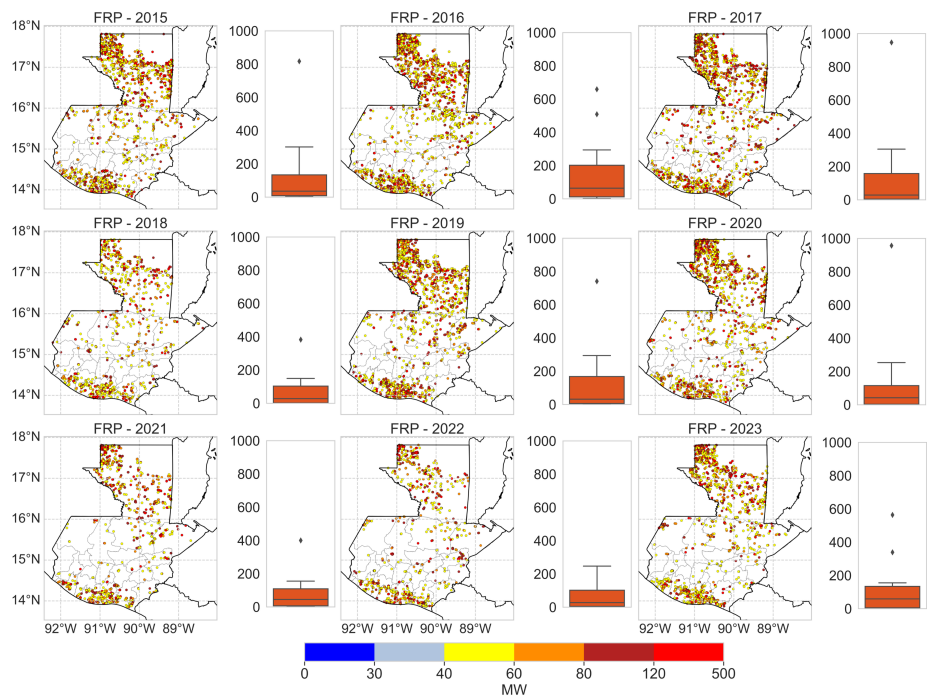
**Figure 5: Mean monthly fire counts distribution and boxplot of detected fires over Guatemala (2015–2023), filtered by nominal
confidence level >70% and fire radiative power >40 MW, values represent the annual distribution of fire activity.**

380   The spatial distribution and box plots illustrate the monthly fires activity in Guatemala (Fig. 6). A clear seasonal pattern in fire
occurrence is obvious. Fire activity is relatively low at the start of the year, with a monthly mean of 77 fires in January
(maximum of 114), gradually increasing in February to a mean of 105 fires (maximum 144). A substantial rise in fire activity
occurs in March, with a mean of 211 fires (maximum 305). April marks the peak of fire activity, recording the highest monthly
mean of 635 fires and the highest maximum of 957 fires indicating the strongest variability and largest IQR. Although fire
385   activity remains elevated in May, with a mean of 261 fires (maximum 509), before declining sharply in June to a mean of 15
fires and a maximum of 69. The lowest fire activity occurs in September, with a mean of 3 fires and a maximum of only 5
until a slight increase in fire activity returns from December (mean of 46, maximum of 64). The remaining months, July to
November, generally exhibit low fire activity, with monthly means below 15 fires (Table S4).

390   The spatial distribution of FRP across Guatemala also confirms this seasonal pattern and shows the shifts in fire location and intensity. During the early months of the year, from January to March, fire activity is concentrated mainly in the southern regions, particularly in the department of Escuintla and adjacent lowland areas. As the season advances, fire activity shifts northward reaching a peak in April. During this period, both the intensity and spatial extent of fires increase markedly with widespread high-intensity events, particularly across the northern and central regions. From June onwards, a decrease in FRP

395   hotspot areas is evident. Fire activity decreases substantially, with only a few moderate-intensity events observed in localized areas in the northern part (department of Petén). This trend continues through the later months of the year, from July to October, when fire activity reaches its minimum. In November and December fire activity remerged marking the beginning of the next fire season.
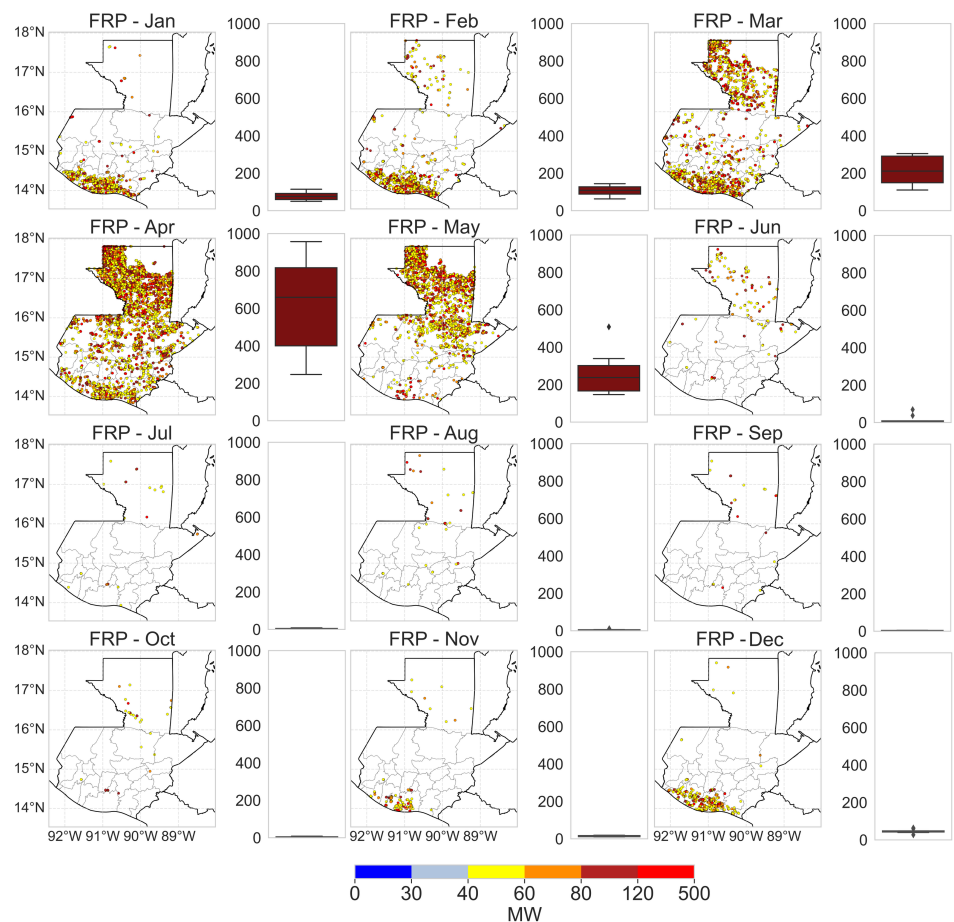
400

Figure 6: Mean monthly fire counts distribution and boxplot of detected fires over Guatemala (2015–2023), filtered by nominal confidence level >70% and fire radiative power >40 MW, values represent the annual distribution of fire activity.

3.4 Meteorology

405 Figure 7 illustrates the time series of monthly NH_3 concentrations, planetary boundary layer height (m), temperature (°C), relative humidity (%), and total precipitation (mm) from 2015 to 2023. All the variables exhibit a clear seasonal pattern, with NH_3 concentrations and PBLH generally peaking in the middle of each year, which points to a general inverse relationship where higher NH_3 concentrations tend to coincide with lower PBLH values, and vice versa. This pattern suggests that a shallower boundary layer, which restricts the vertical dispersion, leads to an accumulation of NH_3 near the surface.

410
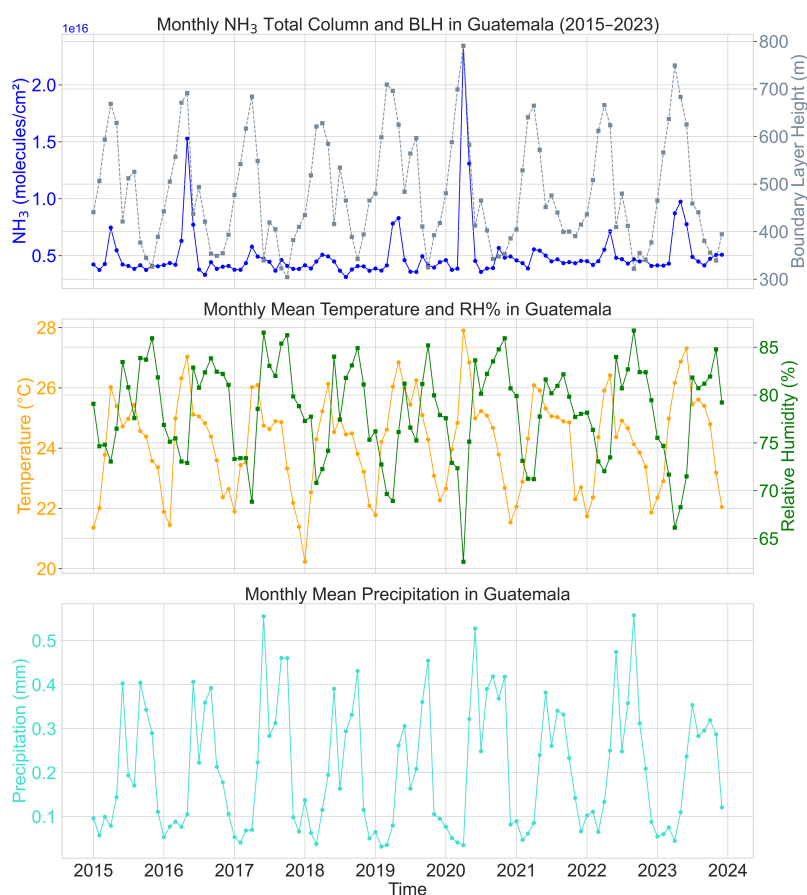
Figure 7: Time series of NH₃ emission (blue line) and meteorological monthly means in Guatemala of atmospheric planetary boundary layer height (PBLH) (light gray line), relative humidity (%) (green line), temperature (°C) (yellow line) and precipitation (mm) (turquoise line).

415

3.5 Case Study of NH₃ Emission

NH₃ anomalies were observed in Guatemala in April 2020, marking the highest emission levels recorded during the study period with a monthly means detected by IASI A (2.32×10^{16} molecules/cm^2), B (2.48×10^{16} molecules/cm^2) and C (2.43×10^{16} molecules/cm^2). This peak is particularly noteworthy as it occurred shortly after the implementation of COVID-19

420   lockdown measures in March 2020, which significantly reduced transportation and industrial activity (Fig. S4).

The monthly mean spatial distribution of NH₃ during April 2020 reveals distinct hotspots concentrated in the northern and southern regions of Guatemala. The most affected location is the department of Petén (max. 7.8×10^{16} molecules/cm^2) and Quiché. Furthermore, In May, a hotspot emerged in the southern, particularly in the department of Escuintla, where

425   concentration reached 5.9×10^{16} molecules/cm^2 (Fig. 8).

The corresponding environmental conditions, including wind vectors meter over second (m/s), further clarify the dynamics of NH₃ dispersion. Strong easterly winds (~3 m/s) dominated the northern region, facilitating long-range transport of NH₃, while central Guatemala experienced moderate to stagnant wind conditions that likely favored local accumulation. Similarly, wind

430   patterns were present in March and May 2020, although wind speed decreased in May. Notably, the increase in NH₃ concentrations in southern Guatemala during May coincided with weaker wind activity.
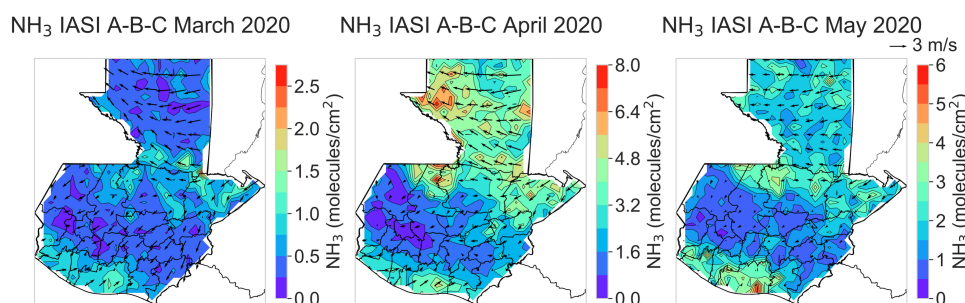
Figure 8: Monthly mean area-wide of NH₃ ($\times 10^{16}$ molecules/cm^2) with wind mean vectors over Guatemala (March, April and May

435   **2020).**

To disentangle surface driven emissions from atmospheric transport mechanisms, we analyzed the vertical and latitudinal distribution of atmospheric NH₃ using zonal means and vertical profiles over Guatemala. This approach allows us to assess surface emissions, transport, and dilution processes. Figure 9a shows a cross-section of NH₃ mass mixing ratios throughout

440   the atmosphere (model level 60 to 44) along the latitudes of Guatemala as a zonal mean. It highlights a greater abundance of NH₃ in both the northern and southern regions, with concentrations primarily confined to the lower atmospheric levels. Furthermore, the NH₃ concentrations vary with both latitude and altitude, the highest concentrations of NH₃ are observed at lower model levels (below approximately level 45), this demonstrates that NH₃ is primarily concentrated near the surface.

Specifically, the highest mass mixing ratios are found between 14°N and 15°N latitude, while north of 15°N the NH₃
445   concentration decreases with increasing latitude and at latitudes south of 14°N, the plot shows lower concentrations.

Fig. 9b further illustrates the area-average vertical profiles of NH₃ concentrations for April (blue line), spring (March – May,
green line) and the entire year 2020 (black dashed line). The vertical axis is represented in model levels, where level 60
corresponds to the surface and decreasing levels indicate increasing altitude in the model coordinate system. While model
450   levels are not fixed to physical altitudes, model level 60 typically corresponds to near-surface conditions (~0–100 m), and
model level 40 is approximately situated around 5–7 km above sea level, depending on surface pressure and atmospheric
stratification. The vertical profile of NH₃ shows the April 2020 mean (blue line) with 1.93×10^{-3} parts per million by volume
(PPMV) (~4.0×10^{16} molecules/cm²), the spring mean (March–May 2020, green line) of 1.55×10^{-3} PPMV (~3.3×10^{16}
molecules/cm²) and the annual mean for 2020 (black dashed line) with 0.90×10^{-3} PPMV (~1.9×10^{16} molecules/cm²)
455   respectively. The profile reveals that NH₃ concentrations were highest near the surface (model level 60) during April, gradually
decreasing with altitude, likely due to dilution as emissions dispersed upward mainly driven by intense wildfire activity during
this period.
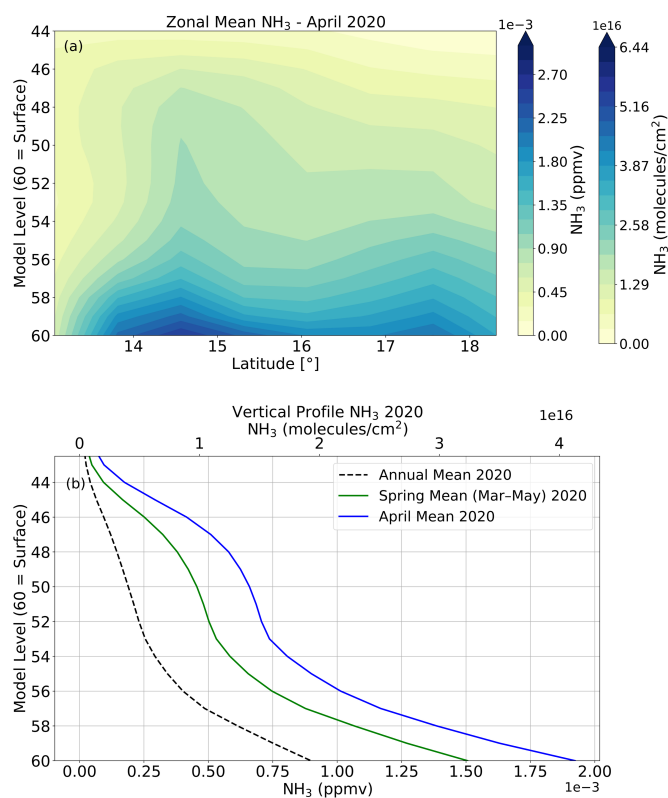
460   **Figure 9: (a) zonal mean mass mixing ration across latitudinal bands (model level 60 to 44) for April 2020 and (b) vertical profile of
NH₃ for April (blue line), spring (March – May, green line) and the entire year 2020 (black dashed line) over Guatemala.**

3.6 Fires and burned areas

Fire activity in spring 2020 showed an anomalous peak compared to the long-term pattern. As mentioned above, March to
465 May indicate a general peak phase in fire activities in Guatemala. With respect to spring 2020. April 2020 recorded the highest number of active fires across Guatemala throughout the entire study period (957), representing a significant anomaly in the observed annual cycle (Fig. 10a). The FRP distribution illustrate this anomaly, in April, fires were not only more numerous but also more spatial extensive, covering both the northern lowlands (Petén) and the central regions of Guatemala, with many highly intensive events (>100 MW). By contrast, March fires were fewer and spatially scattered, while May showed a decline
470 in both intensity and spatial coverage, though localized cluster persisted, particularly in the department of Alta Verapaz (central north) (Fig. 10b). This spatial and temporal concentration of intense fire activity in April 2020 coincides with the exceptional NH_3 anomalies observed during the same month.

This case study demonstrates that April 2020 was not only the climatological peak of the fires season but also exceptionally
475 severe, with both higher-than-average fire intensity and an expanded spatial footprint compared to other years. This assessment of fire intensity and spatial extent was conducted using a confidence level exceeding 70%, thereby enhancing the representativeness and reliability of the observed data.
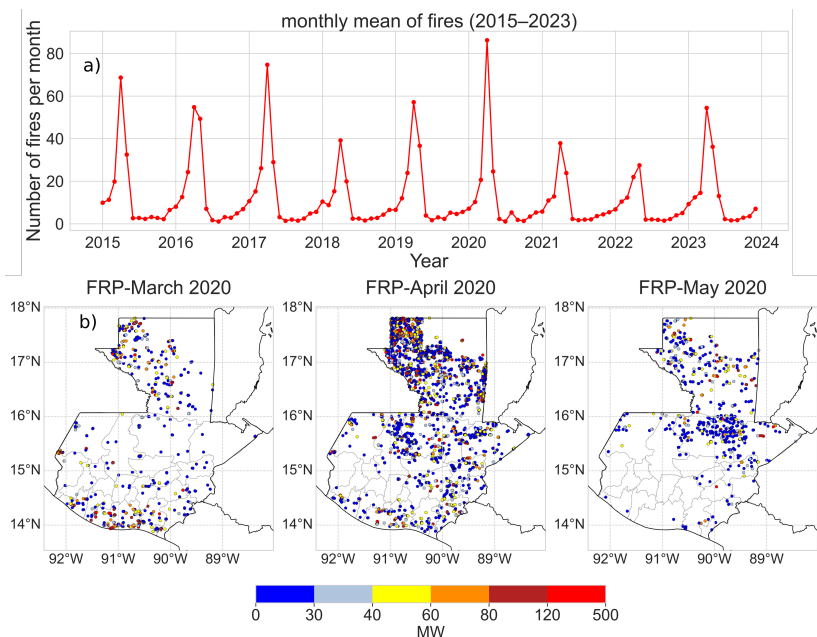
480 **Figure 10: a) Monthly time series of mean fires, and b) area-wide distribution of mean fires over the study period over Guatemala with confidence level over 70%.**

The spatial distribution of burned areas highlights intense fire activity in the northern region of Guatemala (Fig. 11), particularly across multiple days in April 2020. It is striking that the burned areas are located in the northern and southern areas, which are mainly used for agriculture. The most significant burning occurred between April 24 to April 29 when large contiguous burned area were detected located in Petén, covered approximately 53.8 km². The province most severely affected by burned areas was Petén (northern part), suggesting a concentrated fire event during this late-April period. The total burned area between April and May 2020 was approximately 1,485.6 km² (red), representing about 1.36% of Guatemala's national territory.
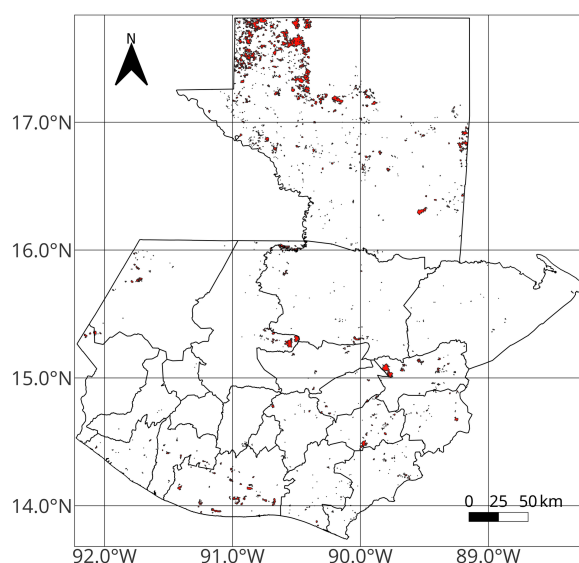
Figure 11: Burned areas during the months of April and May 2020.

4 Discussion

This study investigated the spatiotemporal dynamics of atmospheric NH₃ emissions from IASI A/B/C sensor data, over Guatemala between 2015–2023 using multi-satellite observations combined with fire, land cover, and meteorological datasets. Based on a case study in April 2020, fire events were linked to agricultural and meteorological anomalies. The observed spatio-temporal variability reflects both consistent long-term patterns and distinct episodic anomalies (Fig. 2). Annual median concentrations remained relatively constant with (4.98×10^{15} molecules/cm²), with limited variability in the interquartile range and overall standard deviations around 1.74×10^{15} molecules/cm². This stability suggests that background NH₃ emissions in Guatemala are relatively constant, likely dominated by persistent sources such as agriculture (fertilizer application and

livestock), which account for the majority of global NH$_3$ emissions (McDuffie et al., 2020; Sutton et al., 2013). Nevertheless, the analysis also identified years with substantially elevated NH$_3$ levels, particularly 2016, 2020, and 2023, which exhibited both higher annual means and extreme values. Among these years, 2020 recorded the highest annual average (6.67×10^{15}

505   molecules/cm^2) and the most extreme single event anomaly (2.34×10^{16} molecules/cm^2) (Table S1).

The seasonal cycle further illustrates this relationship between emissions and seasonal meteorological conditions with concentrations reaching their lowest levels between June–October (Fig. 3). Concentrations were low during October–December (mean $\sim 4.3 \times 10^{15}$ molecules/cm^2, maximum mean $>1.6 \times 10^{16}$ molecules cm^2), but increased steadily from January,

510   peaking in April–May (mean $\sim 1.0 \times 10^{16}$ molecules/cm^2, maximum mean $>2.3 \times 10^{16}$ molecules cm^2). This period corresponds with the Central American fire season, during which NH$_3$ emissions intensify. Following this peak, the monthly mean NH$_3$ concentrations decreased dramatically by approximately 42.0% in June. The sharp decline after June reflects the onset of the rainy season, when fires diminish and wet deposition increases (Ríos and Raga, 2018). Persistent NH$_3$ hotspots were detected in the northern (Petén, and Quiché, mean $\sim 2.2 \times 10^{16}$ molecules/cm^2) and southern (Escuintla, mean $\sim 2.1 \times 10^{16}$ molecules/cm^2)

515   areas of Guatemala characterized by intensive cropland, rangeland, and repeated fires occurrence across years. In contrast, the highlands and central regions showed lower values (mean $\sim 5.0 \times 10^{15}$ molecules/cm^2). Even in relatively low-emission years such as 2018 (annual mean 4.12×10^{15} molecules cm^2), localized southern hotspots persisted during the fire season, underlining the influence of spatially concentrated emission sources. These findings align with global studies showing strong seasonal patterns in NH$_3$ emissions, reflecting fertilizer application timing and biomass burning (Van Damme et al., 2018, 2021;

520   Fortems-Cheiney et al., 2016; Saravia and Trachte, 2025). The results highlight that while agriculture provides a stable emission baseline, episodic fire activity acts as a seasonal amplifier of NH$_3$ variability.

The cluster analysis further highlights the strong influence of land cover composition on NH$_3$ variability across Guatemala (Fig. 4). Particularly Cluster 1, dominated by cropland and rangeland, consistently exhibited the highest concentrations,

525   reinforcing the role of fertilizer application and livestock as persistent emission sources. Although it covers the smallest area, its intensively managed agricultural mosaics contributed disproportionately to national emissions, demonstrating how local land-use practices can have regional impacts on the atmosphere. In contrast, Cluster 2 (extensive forest and transitional agriculture) and Cluster 3 (urban, rangeland, forest areas) showed moderate and low NH$_3$ levels, respectively. The observed gradient among clusters suggests that agricultural intensity, rather than the presence of urbanization or semi-natural landscapes,

530   primarily drive the NH$_3$ variability. Comparable spatial patterns have been reported for other agricultural regions, like South Asia, where cropland dominated areas exhibited enhanced NH$_3$ emission (Abeed et al., 2022). Also, in Western Europe higher levels of NH$_3$ were found which were linked to intensive livestock production and the use of fertilizer (Van Damme et al., 2018). Moreover, small but intensively managed cropland and rangeland mosaics disproportionately contribute to national emissions, reinforcing the role of regional hotspots. The temporal overlap of maximum NH$_3$ concentrations with fire counts

535   and FRP underscores biomass burning as a major episodic source (Fig. 5). Peak years such as 2016, 2017, and 2020 mirrored

elevated NH₃ anomalies, while reduced fire activity in 2018 and 2021–2022 coincided with lower emissions. Similar patterns were reported for Amazonia, where NH₃ emission from biomass burning exhibit strong spatial and temporal variability, with interannual peak linked to severe droughts and late fire-season activity, highlighting the influence of El Niño-Southern Oscillation (ENSO) events (Whitburn et al., 2017) and Southeast Asia, particularly Indonesia, largely human-induced fires for

540   land clearing burned extensive tropical forest and peatlands, releasing substantial NH₃ emissions, which were further amplified by strong ENSO conditions (Chang et al., 2021; Whitburn et al., 2016b).

Guatemalan fire driven NH₃ peaks appear to be predominantly human caused. (FAO, 2007) reports that most fires worldwide are anthropogenic, and in Central America, lightning is minimal during November–April, precisely when fire activity is highest

545   (Kucieńska et al., 2010). Practices such as burning to stimulate pasture regrowth, suppress vegetation, and prepare cropland (Keeley, 2002) likely explain this seasonality. However, a clear interannual variability in both fire counts and intensity, could be observed (Fig. 5). 2016 and 2017 recorded the highest fire frequencies, with 2017 also producing the most extreme monthly peak before 2020. In contrast 2018 and 2022 were marked by sharp declines in activity. The elevated fire activity in 2016–2017 coincided with warmer and relatively drier conditions across Guatemala. Annual mean temperatures reached 24.16 °C

550   (2016) and 23.9 °C (2017) as shown in Fig. S5, consistent with (INSIVUMEH, 2023) ground observations of 24.5°C and 24.3°C, respectively. Similarly, precipitation totals were below average, indicating 0.19–0.23 mm day⁻¹ (Fig. S6) and INSIVUMEH reporting 1850–2100 mm year⁻¹, compared to wetter years such as 2020 and 2022 (>2300 mm year⁻¹). These conditions followed the 2015–2016 ENSO episode (Anderson et al., 2023), which induced drought stress and elevated surface temperatures throughout Guatemala, thereby increasing fire susceptibility. Similar ENSO driven fire and NH₃ anomalies have

555   been reported in other tropical regions. Particularly in Indonesia, where Whitburn et al. (2016) documented a doubling of annual NH₃ emissions during the 2015 El Niño due to extensive peatland fires. Such ENSO related drought anomalies have been shown to intensify biomass burning and NH₃ emissions by reducing vegetation moisture and fuel humidity (Burton et al., 2020). In contrast, cooler and wetter years such as 2018 and 2022 coincided with reduced fire activity and lower NH₃ emissions, emphasizing that meteorological variability modulated by ENSO phases.

560

To further illustrate this fire–NH₃ connections under contrasting meteorological conditions, the most extreme fire anomaly during the study period (April 2020, Fig.10) was selected for detailed analysis. This month exhibited exceptionally high fire counts and FRP, corresponding with a pronounced NH₃ peak record. Especially in the northern (Petén) and southern (Escuintla) regions, fire occurrences reached up to 957 hotspots, confirming the spatial coincidence between biomass burning and

565   enhanced NH₃ concentrations. This event represents a critical episode of regionally intensified emissions, likely driven by prolonged dry conditions during April 2020, despite being characterized by near-neutral ENSO conditions (annual precipitation in 2020 = 2,350 mm, INSIVUMEH) and above the average temperatures (24.6 °C). According to INSIVUMEH, 2020 was the third hottest year of the study period and recorded the highest total precipitation. Moreover, the atmospheric

boundary layer height during April 2020 exhibited one of the lowest mixing layer heights of the entire period (Fig. 7), which

570   likely contributed to the accumulation and enhanced detection of NH_3 emissions in the lower atmosphere.

Despite reduced traffic and industrial activity under COVID-19 lockdowns, NH_3 concentrations reached unprecedented levels due to widespread, intense fires activity (Fig. S4). Meteorological conditions during this period showed that emissions remained confined to the lower troposphere, below model level 54 (altitude approximately <1 km), indicating surface-driven

575   emissions with limited vertical mixing, which favors the accumulation of NH_3 (Fig. 9). Weak wind circulation during April 2020 further constrain dispersion, particularly across the central and northern regions, enhancing the local emissions. Overall, approximately 1,486 km^2 were affected (1.36% of national territory), mostly in agricultural landscapes (Petén) (Fig. 11). Notably, most of these burned areas were located in the northwest of Guatemala, within the officially designated protected areas that correspond to the large Maya Biosphere reserve (CONAP, 2016), underscoring the ecological and regulatory

580   implications of such extreme events.

5 Conclusion

This study provides the first integrated spatiotemporal assessment of atmospheric NH_3 emissions over Guatemala (2015–2023), using multi-satellite observations combined with fire, land cover, and meteorological reanalysis data. The results reveal

585   distinct seasonal and interannual patterns, with NH_3 concentrations peaking in April–May during the regional fire season and declining sharply after the onset of rainfall. Interannual variability was characterized by pronounced anomalies in 2016, 2020, and 2023, reflecting the combined influence of fire activity and climatic variability. Additionally, persistent hotspots were detected in the northern (Petén–Quiché) and southern (Escuintla) agricultural regions, driven by intensive use of fertilizer, livestock and widespread anthropogenic biomass burning. These agricultural areas contribute disproportionately to Guatemala

590   NH_3 emissions despite their smaller spatial extent.

The analysis also highlights the role of meteorology and ENSO related anomalies in modulating NH_3 variability. Warm ENSO phases (2015–2016 and 2023) enhanced drought stress and fire susceptibility, while favorable meteorological conditions such as high temperature and shallow boundary layers intensified NH_3 accumulation. The April 2020 case study exemplified the

595   linking between fire activity and NH_3 emissions, when nearly 1,500 km^2 burned and concentrations reached their highest levels of the entire record. This episode occurred under near neutral ENSO conditions but was reinforced by locally extreme dryness, low boundary layer height and reduced anthropogenic activity during the COVID-19 lockdown, leading to enhanced NH_3 retention in the atmosphere.

600 Overall, the findings demonstrate a dual emission regime over Guatemala, with a stable agricultural baseline overlaid by episodic peaks due to fires, which are modulated by climatic variability. Continuous satellite-based monitoring remains essential for improving emission inventories, supporting regional air quality management, and guiding strategies to reduce biomass burning impacts. Uncertainties remain regarding the quantification of absolute emission and the role of smaller scale or undocumented burning. Future work should integrate ground-based observations, finer resolution land use data, and

605 atmospheric modeling to better constrain source contribution and transport process to understand the role of NH_3 as a precursor to particulate matter and broader climate impacts in Central America.

Data availability

Monthly atmospheric ammonia column products from the Infrared Atmospheric Sounding Interferometer (IASI A/B/C),

610 versioned Level-3 data cover global grids, AERIS-IASI portal: https://iasi.aeris-data.fr/nh3/. Monthly atmospheric variables are provided by the ERA5 reanalysis dataset (https://cds.climate.copernicus.eu/datasets/reanalysis-era5-single-levels-monthly-means?tab=download). Active fire detections MODIS-Aqua/Terra from the NASA-Earth Observing System's Fire Information for Resource Management System (FIRMS) database (https://firms.modaps.eosdis.nasa.gov/). Burned area monthly L3 global 500m grid V061 (https://www.earthdata.nasa.gov/data/catalog/lpcloud-mcd64a1-061).

615 **Author contributions**

Conceptualization, C.S. and K.T.; methodology, C.S. and K.T.; formal analysis, C.S.; investigation, C.S. and P.S.; resources, C.S. and P.S.; data curation, C.S.; writing (original draft preparation), C.S.; writing (review and editing), C.S., P.S., and K.T.; visualization, C.S.; supervision, K.T.

Competing interest

620 The authors declare that they have no conflict of interest.

Financial support

This research received no external funding.

References

625 Abeed, R., Viatte, C., Porter, W. C., Evangeliou, N., Clerbaux, C., Clarisse, L., Van Damme, M., Coheur, P.-F., and Safieddine, S.: Estimating agricultural ammonia volatilization over Europe using satellite observations and simulation data, EGUsphere, https://doi.org/10.5194/egusphere-2022-1046, 2022.

Ahmad, A. and Dey, L.: A k-mean clustering algorithm for mixed numeric and categorical data, Data Knowl Eng, 63, 503–527, https://doi.org/10.1016/j.datak.2007.03.016, 2007.

630 Alfaro Marroquín, G. and Gómez, R.: Antecedentes y contexto del cambio climático en Guatemala, in: Primer reporte de evaluación del conocimiento sobre cambio climático en Guatemala, edited by: Castellanos, E. J., Paiz-Estévez, A., Escribá, J., Rosales-Alconero, M., and Santizo, A., Editorial Universitaria UVG, Guatemala, 2–19, 2019.

Anderson, T. G., McKinnon, K. A., Pons, D., and Anchukaitis, K. J.: How Exceptional Was the 2015–2019 Central American Drought?, Geophys Res Lett, 50, https://doi.org/10.1029/2023GL105391, 2023.

635 Andreae, M. O.: Emission of trace gases and aerosols from biomass burning – an updated assessment, Atmos Chem Phys, 19, 8523–8546, https://doi.org/10.5194/acp-19-8523-2019, 2019.

Anne Fouilloux: annefou/metos_python: Working with Spatio-temporal data in Python (v2018.0.0), https://doi.org/doi.org/10.5281/zenodo.1165281, 2018.

Bardales Espinoza, W. A., Castañón, C., and Herrera Herrera, J. L.: Clima de Guatemala, tendencias observadas e índices de 640 cambio climático, in: Primer reporte de evaluación del conocimiento sobre cambio climático en Guatemala, vol. 1, edited by: Castellanos, E. J., Paiz-Estévez, A., Escribá J., Rosales-Alconero M., and Santizo A., Editorial Universitaria UVG, Guatemala, 20–39, 2019.

Burton, C., Betts, R. A., Jones, C. D., Feldpausch, T. R., Cardoso, M., and Anderson, L. O.: El Niño Driven Changes in Global Fire 2015/16, Front Earth Sci (Lausanne), 8, https://doi.org/10.3389/feart.2020.00199, 2020.

645 Chang, Y., Zhang, Y.-L., Kawichai, S., Wang, Q., Van Damme, M., Clarisse, L., Prapamontol, T., and Lehmann, M. F.: Convergent evidence for the pervasive but limited contribution of biomass burning to atmospheric ammonia in peninsular Southeast Asia, Atmos Chem Phys, 21, 7187–7198, https://doi.org/10.5194/acp-21-7187-2021, 2021.

Chen, J., Cheng, M., Krol, M., de Vries, W., Zhu, Q., Liu, X., Zhang, F., and Xu, W.: Trends in anthropogenic ammonia emissions in China since 1980: A review of approaches and estimations, Front Environ Sci, 11, 650 https://doi.org/10.3389/fenvs.2023.1133753, 2023.

Chen, P. and Wang, Q.: Underestimated industrial ammonia emission in China uncovered by material flow analysis, Environmental Pollution, 368, 125740, https://doi.org/10.1016/j.envpol.2025.125740, 2025.

Chen, P., Wang, Q., Shao, M., and Liu, R.: Significantly underestimated traffic-related ammonia emissions in Chinese megacities: Evidence from satellite observations during COVID-19 lockdowns, Chemosphere, 361, 142497, https://doi.org/10.1016/j.chemosphere.2024.142497, 2024.

Chuvieco, E., Mouillot, F., van der Werf, G. R., San Miguel, J., Tanase, M., Koutsias, N., García, M., Yebra, M., Padilla, M., Gitas, I., Heil, A., Hawbaker, T. J., and Giglio, L.: Historical background and current developments for mapping burned area from satellite Earth observation, Remote Sens Environ, 225, 45–64, https://doi.org/10.1016/j.rse.2019.02.013, 2019.

Clarisse, L., Clerbaux, C., Dentener, F., Hurtmans, D., and Coheur, P.-F.: Global ammonia distribution derived from infrared satellite observations, Nat Geosci, 2, 479–483, https://doi.org/10.1038/ngeo551, 2009.

Clarisse, L., Shephard, M. W., Dentener, F., Hurtmans, D., Cady-Pereira, K., Karagulian, F., Van Damme, M., Clerbaux, C., and Coheur, P.: Satellite monitoring of ammonia: A case study of the San Joaquin Valley, Journal of Geophysical Research: Atmospheres, 115, https://doi.org/10.1029/2009JD013291, 2010.

Clarisse, L., Van Damme, M., Clerbaux, C., and Coheur, P.-F.: Tracking down global NH3 point sources with wind-adjusted super resolution, Atmos Meas Tech, 12, 5457–5473, https://doi.org/10.5194/amt-12-5457-2019, 2019.

Clarisse, L., Franco, B., Van Damme, M., Di Gioacchino, T., Hadji-Lazaro, J., Whitburn, S., Noppen, L., Hurtmans, D., Clerbaux, C., and Coheur, P.: The IASI NH$_3$ version 4 product: averaging kernels and improved consistency, Atmos Meas Tech, 16, 5009–5028, https://doi.org/10.5194/amt-16-5009-2023, 2023.

Coheur, P.-F., Clarisse, L., Turquety, S., Hurtmans, D., and Clerbaux, C.: IASI measurements of reactive trace species in biomass burning plumes, Atmos Chem Phys, 9, 5655–5667, https://doi.org/10.5194/acp-9-5655-2009, 2009.

CONAP: Ley de Áreas Protegidas y su Reglamento, Decreto No. 4-89 y sus Reformas, Decretos No. 18-89, 110-96 y 111-97 del Congreso de la República de Guatemala, 114, 2016.

CONRED: Protocolo Nacional Temporada de Incendios Forestales y No Forestales, Guatemala, 3–83 pp., 2025.

Van Damme, M., Whitburn, S., Clarisse, L., Clerbaux, C., Hurtmans, D., and Coheur, P.-F.: Version 2 of the IASI NH3 neural network retrieval algorithm: near-real-time and reanalysed datasets, Atmos Meas Tech, 10, 4905–4914, https://doi.org/10.5194/amt-10-4905-2017, 2017.

Van Damme, M., Clarisse, L., Whitburn, S., Hadji-Lazaro, J., Hurtmans, D., Clerbaux, C., and Coheur, P.-F.: Industrial and agricultural ammonia point sources exposed, Nature, 564, 99–103, https://doi.org/10.1038/s41586-018-0747-1, 2018.

Van Damme, M., Clarisse, L., Franco, B., Sutton, M. A., Erisman, J. W., Wichink Kruit, R., van Zanten, M., Whitburn, S.,
680 Hadji-Lazaro, J., Hurtmans, D., Clerbaux, C., and Coheur, P.-F.: Global, regional and national trends of atmospheric ammonia
derived from a decadal (2008–2018) satellite record, Environmental Research Letters, 16, 055017,
https://doi.org/10.1088/1748-9326/abd5e0, 2021.

Van Damme, M., Clarisse, L., Stavrakou, T., Wichink Kruit, R., Sellekaerts, L., Viatte, C., Clerbaux, C., and Coheur, P. F.:
On the weekly cycle of atmospheric ammonia over European agricultural hotspots, Sci Rep, 12,
685 https://doi.org/10.1038/s41598-022-15836-w, 2022.

Dammers, E., Palm, M., Van Damme, M., Vigouroux, C., Smale, D., Conway, S., Toon, G. C., Jones, N., Nussbaumer, E.,
Warneke, T., Petri, C., Clarisse, L., Clerbaux, C., Hermans, C., Lutsch, E., Strong, K., Hannigan, J. W., Nakajima, H., Morino,
I., Herrera, B., Stremme, W., Grutter, M., Schaap, M., Wichink Kruit, R. J., Notholt, J., Coheur, P.-F., and Erisman, J. W.: An
evaluation of IASI-NH3 with ground-based Fourier transform infrared spectroscopy measurements, Atmos Chem Phys, 16,
690 10351–10368, https://doi.org/10.5194/acp-16-10351-2016, 2016.

Dong, Z. P., Yu, X., Li, X. M., and Dai, J.: Analysis of variation trends and causes of aerosol optical depth in Shaanxi Province
using MODIS data, Chinese Science Bulletin, 58, 4486–4496, https://doi.org/10.1007/S11434-013-5991-Z, 2013.

Dragosits, U., Theobald, M. R., Place, C. J., Lord, E., Webb, J., Hill, J., ApSimon, H. M., and Sutton, M. A.: Ammonia
emission, deposition and impact assessment at the field scale: a case study of sub-grid spatial variability, Environmental
695 Pollution, 117, 147–158, https://doi.org/10.1016/S0269-7491(01)00147-6, 2002.

ESRI: ESRI: Sentinel-2 2020 Global Land Use/Land Cover (LULC) Map, 12 pp., 2021.

European Space Agency: Copernicus Global Digital Elevation Model, https://doi.org/https://doi.org/10.5069/G9028PQB,
2024.

Evangeliou, N., Balkanski, Y., Eckhardt, S., Cozic, A., Van Damme, M., Coheur, P.-F., Clarisse, L., Shephard, M. W., Cady-
700 Pereira, K. E., and Hauglustaine, D.: 10-year satellite-constrained fluxes of ammonia improve performance of chemistry
transport models, Atmos Chem Phys, 21, 4431–4451, https://doi.org/10.5194/acp-21-4431-2021, 2021.

FAO: Fire Management - Global Assessment 2006, 135 pp., 2007.

FAO: FAOSTAT. Countries by commodity, 2019.

Farren, N. J., Davison, J., Rose, R. A., Wagner, R. L., and Carslaw, D. C.: Underestimated Ammonia Emissions from Road
705 Vehicles, Environ Sci Technol, 54, 15689–15697, https://doi.org/10.1021/acs.est.0c05839, 2020.

Farren, N. J., Davison, J., Rose, R. A., Wagner, R. L., and Carslaw, D. C.: Characterisation of ammonia emissions from gasoline and gasoline hybrid passenger cars, Atmos Environ X, 11, 100117, https://doi.org/10.1016/j.aeaoa.2021.100117, 2021.

Flemming, J., Benedetti, A., Inness, A., Engelen, R. J., Jones, L., Huijnen, V., Remy, S., Parrington, M., Suttie, M., Bozzo, A., Peuch, V.-H., Akritidis, D., and Katragkou, E.: The CAMS interim Reanalysis of Carbon Monoxide, Ozone and Aerosol for 2003–2015, Atmos Chem Phys, 17, 1945–1983, https://doi.org/10.5194/acp-17-1945-2017, 2017.

Fortems-Cheiney, A., Dufour, G., Hamaoui-Laguel, L., Foret, G., Siour, G., Van Damme, M., Meleux, F., Coheur, P. -F., Clerbaux, C., Clarisse, L., Favez, O., Wallasch, M., and Beekmann, M.: Unaccounted variability in NH3 agricultural sources detected by IASI contributing to European spring haze episode, Geophys Res Lett, 43, 5475–5482, https://doi.org/10.1002/2016GL069361, 2016.

Franco, B., Clarisse, L., Stavrakou, T., Müller, J. -F, Van Damme, M., Whitburn, S., Hadji-Lazaro, J., Hurtmans, D., Taraborrelli, D., Clerbaux, C., and Coheur, P. -F: A General Framework for Global Retrievals of Trace Gases From IASI: Application to Methanol, Formic Acid, and PAN, Journal of Geophysical Research: Atmospheres, 123, https://doi.org/10.1029/2018JD029633, 2018.

Freeborn, P. H., Wooster, M. J., and Roberts, G.: Addressing the spatiotemporal sampling design of MODIS to provide estimates of the fire radiative energy emitted from Africa, Remote Sens Environ, 115, 475–489, https://doi.org/10.1016/j.rse.2010.09.017, 2011.

Fu, Y., Li, R., Wang, X., Bergeron, Y., Valeria, O., Chavardès, R. D., Wang, Y., and Hu, J.: Fire Detection and Fire Radiative Power in Forests and Low-Biomass Lands in Northeast Asia: MODIS versus VIIRS Fire Products, Remote Sens (Basel), 12, 2870, https://doi.org/10.3390/rs12182870, 2020.

Gašparović, M., Zrinjski, M., and Gudelj, M.: Automatic cost-effective method for land cover classification (ALCC), Comput Environ Urban Syst, 76, 1–10, https://doi.org/10.1016/j.compenvurbsys.2019.03.001, 2019.

Giglio, L., Descloitres, J., Justice, C. O., and Kaufman, Y. J.: An Enhanced Contextual Fire Detection Algorithm for MODIS, Remote Sens Environ, 87, 273–282, https://doi.org/10.1016/S0034-4257(03)00184-6, 2003.

Giglio, L., van der Werf, G. R., Randerson, J. T., Collatz, G. J., and Kasibhatla, P.: Global estimation of burned area using MODIS active fire observations, Atmos Chem Phys, 6, 957–974, https://doi.org/10.5194/acp-6-957-2006, 2006.

Giglio, L., Randerson, J. T., and van der Werf, G. R.: Analysis of daily, monthly, and annual burned area using the fourth-generation global fire emissions database (GFED4), J Geophys Res Biogeosci, 118, 317–328, https://doi.org/10.1002/jgrg.20042, 2013.

735   Giglio, L., Schroeder, W., and Justice, C. O.: The collection 6 MODIS active fire detection algorithm and fire products, Remote Sens Environ, 178, 31–41, https://doi.org/10.1016/j.rse.2016.02.054, 2016.

Giglio, L., Boschetti, L., Roy, D. P., Humber, M. L., and Justice, C. O.: The Collection 6 MODIS burned area mapping algorithm and product, Remote Sens Environ, 217, 72–85, https://doi.org/10.1016/j.rse.2018.08.005, 2018.

Giglio, L., Schroeder, W., Hall, J. V., and Justice, C. O.: MODIS Collection 6 and Collection 6.1 Active Fire Product User's
740   Guide, 2021a.

Giglio, L., Justice, C., Boschetti, L., and Roy, D.: MODIS/Terra + Aqua Burned Area Monthly L3 Global 500 m SIN Grid V061, NASA EOSDIS Land Processes DAAC [data set], https://doi.org/https://doi.org/10.5067/MODIS/MCD64A1.061, 2021b.

Gu, C., Wang, S., Zhu, J., Dai, W., Liu, J., Xue, R., Che, X., Lin, Y., Duan, Y., Wenig, M. O., and Zhou, B.: Underestimated
745   ammonia vehicular emissions in metropolitan city revealed by on-road mobile measurement, Environmental Research Letters, 18, 104040, https://doi.org/10.1088/1748-9326/acf94a, 2023.

Guo, Y., Hong, S., Feng, N., Zhuang, Y., and Zhang, L.: Spatial distributions and temporal variations of atmospheric aerosols and the affecting factors: a case study for a region in central China, Int J Remote Sens, 33, 3672–3692, https://doi.org/10.1080/01431161.2011.631951, 2012.

750   Hantson, S., Padilla, M., Corti, D., and Chuvieco, E.: Strengths and weaknesses of MODIS hotspots to characterize global fire occurrence, Remote Sens Environ, 131, 152–159, https://doi.org/10.1016/j.rse.2012.12.004, 2013.

Herrera, B., Bezanilla, A., Blumenstock, T., Dammers, E., Hase, F., Clarisse, L., Magaldi, A., Rivera, C., Stremme, W., Strong, K., Viatte, C., Van Damme, M., and Grutter, M.: Measurement report: Evolution and distribution of NH3 over Mexico City from ground-based and satellite infrared spectroscopic measurements, Atmos Chem Phys, 22, 14119–14132,
755   https://doi.org/10.5194/acp-22-14119-2022, 2022.

Hersbach, H., Bell, B., Berrisford, P., Hirahara, S., Horányi, A., Muñoz-Sabater, J., Nicolas, J., Peubey, C., Radu, R., Schepers, D., Simmons, A., Soci, C., Abdalla, S., Abellan, X., Balsamo, G., Bechtold, P., Biavati, G., Bidlot, J., Bonavita, M., De Chiara, G., Dahlgren, P., Dee, D., Diamantakis, M., Dragani, R., Flemming, J., Forbes, R., Fuentes, M., Geer, A., Haimberger, L., Healy, S., Hogan, R. J., Hólm, E., Janisková, M., Keeley, S., Laloyaux, P., Lopez, P., Lupu, C., Radnoti, G., de Rosnay, P.,
760   Rozum, I., Vamborg, F., Villaume, S., and Thépaut, J.: The ERA5 global reanalysis, Quarterly Journal of the Royal Meteorological Society, 146, 1999–2049, https://doi.org/10.1002/qj.3803, 2020.

Hervas, A.: Land, development and contract farming on the Guatemalan oil palm frontier, J Peasant Stud, 46, 115–141, https://doi.org/10.1080/03066150.2017.1351435, 2019.

IGM: Mapa hipsometrico 2002, Guatemala, 2002.

765 Inness, A., Ades, M., Agustí-Panareda, A., Barré, J., Benedictow, A., Blechschmidt, A.-M., Dominguez, J. J., Engelen, R., Eskes, H., Flemming, J., Huijnen, V., Jones, L., Kipling, Z., Massart, S., Parrington, M., Peuch, V.-H., Razinger, M., Remy, S., Schulz, M., and Suttie, M.: The CAMS reanalysis of atmospheric composition, Atmos Chem Phys, 19, 3515–3556, https://doi.org/10.5194/acp-19-3515-2019, 2019.

INSIVUMEH: Variabilidad y cambio climático en Guatemala, Guatemala, 2018.

770 INSIVUMEH: Estado del Clima en Guatemala, 2023.

Justice, C. O., Giglio, L., Roy, D., Boschetti, L., Csiszar, I., Davies, D., Korontzi, S., Schroeder, W., O'Neal, K., and Morisette, J.: MODIS-Derived Global Fire Products, 661–679, https://doi.org/10.1007/978-1-4419-6749-7_29, 2010.

Karra, K., Kontgis, C., Statman-Weil, Z., Mazzariello, J. C., Mathis, M., and Brumby, S. P.: Global land use / land cover with Sentinel 2 and deep learning, in: 2021 IEEE International Geoscience and Remote Sensing Symposium IGARSS, 4704–4707, 775 https://doi.org/10.1109/IGARSS47720.2021.9553499, 2021.

Keeley, J. E.: Fire Management of California Shrubland Landscapes, Environ Manage, 29, 395–408, https://doi.org/10.1007/s00267-001-0034-Y, 2002.

Kucieńska, B., Raga, G. B., and Rodríguez, O.: Cloud-to-ground lightning over Mexico and adjacent oceanic regions: a preliminary climatology using the WWLLN dataset, Ann Geophys, 28, 2047–2057, https://doi.org/10.5194/angeo-28-2047-780 2010, 2010.

Li, F., Zhang, X., and Kondragunta, S.: Biomass Burning in Africa: An Investigation of Fire Radiative Power Missed by MODIS Using the 375 m VIIRS Active Fire Product, Remote Sens (Basel), 12, 1561, https://doi.org/10.3390/rs12101561, 2020.

Li, J., Hendricks, J., Righi, M., and Beer, C. G.: An aerosol classification scheme for global simulations using the K-means 785 machine learning method, Geosci Model Dev, 15, 509–533, https://doi.org/10.5194/gmd-15-509-2022, 2022.

Liu, Y., Chen, J., Shi, Y., Zheng, W., Shan, T., and Wang, G.: Global Emissions Inventory from Open Biomass Burning (GEIOBB): utilizing Fengyun-3D global fire spot monitoring data, Earth Syst Sci Data, 16, 3495–3515, https://doi.org/10.5194/essd-16-3495-2024, 2024.

Lopez-Ridaura, S., Barba-Escoto, L., Reyna, C., Hellin, J., Gerard, B., and van Wijk, M.: Food security and agriculture in the 790 Western Highlands of Guatemala, Food Secur, 11, 817–833, https://doi.org/10.1007/s12571-019-00940-z, 2019.

Mahata, K., Das, R., Das, S., and Sarkar, A.: Land Use Land Cover map segmentation using Remote Sensing: A Case study of Ajoy river watershed, India, Journal of Intelligent Systems, 30, 273–286, https://doi.org/10.1515/jisys-2019-0155, 2020.

Marais, E. A., Pandey, A. K., Van Damme, M., Clarisse, L., Coheur, P., Shephard, M. W., Cady-Pereira, K. E., Misselbrook, T., Zhu, L., Luo, G., and Yu, F.: UK Ammonia Emissions Estimated With Satellite Observations and GEOS-Chem, Journal
795 of Geophysical Research: Atmospheres, 126, https://doi.org/10.1029/2021JD035237, 2021a.

Marais, E. A., Pandey, A. K., Van Damme, M., Clarisse, L., Coheur, P., Shephard, M. W., Cady-Pereira, K. E., Misselbrook, T., Zhu, L., Luo, G., and Yu, F.: UK Ammonia Emissions Estimated With Satellite Observations and GEOS-Chem, Journal of Geophysical Research: Atmospheres, 126, https://doi.org/10.1029/2021JD035237, 2021b.

McDuffie, E. E., Smith, S. J., O'Rourke, P., Tibrewal, K., Venkataraman, C., Marais, E. A., Zheng, B., Crippa, M., Brauer,
800 M., and Martin, R. V.: A global anthropogenic emission inventory of atmospheric pollutants from sector- and fuel-specific sources (1970–2017): an application of the Community Emissions Data System (CEDS), Earth Syst Sci Data, 12, 3413–3442, https://doi.org/10.5194/essd-12-3413-2020, 2020.

Monzón-Alvarado, C., Cortina-Villar, S., Schmook, B., Flamenco-Sandoval, A., Christman, Z., and Arriola, L.: Land-use decision-making after large-scale forest fires: Analyzing fires as a driver of deforestation in Laguna del Tigre National Park,
805 Guatemala, Applied Geography, 35, 43–52, https://doi.org/10.1016/j.apgeog.2012.04.008, 2012.

Orrego León, E. O., Hernández Quevedo, M. P., and Gómez Jordán, R. C.: Variabilidad del inicio, final y duración de la época lluviosa en Guatemala y su tendencia, Revista Mesoamericana de Biodiversidad y Cambio Climático–Yu'am, 5, 4–24, 2021.

Pan, Y., Tian, S., Liu, D., Fang, Y., Zhu, X., Zhang, Q., Zheng, B., Michalski, G., and Wang, Y.: Fossil Fuel Combustion-Related Emissions Dominate Atmospheric Ammonia Sources during Severe Haze Episodes: Evidence from ^{15}N-Stable Isotope
810 in Size-Resolved Aerosol Ammonium, Environ Sci Technol, 50, 8049–8056, https://doi.org/10.1021/acs.est.6b00634, 2016.

Pedregosa, F., Varoquaux, G., Gramfort, A., Michel, V., Thirion, B., Grisel, O., and Duchesnay, É.: Scikit-learn: Machine learning in Python, the Journal of machine Learning research, 12, 2825–2830, 2011.

Pham, D. T., Dimov, S. S., and Nguyen, C. D.: Selection of K in K-means clustering, Proc Inst Mech Eng C J Mech Eng Sci, 219, 103–119, https://doi.org/10.1243/095440605X8298, 2005.

815 Pohl, V., Gilmer, A., Hellebust, S., McGovern, E., Cassidy, J., Byers, V., McGillicuddy, E. J., Neeson, F., and O'Connor, D. J.: Ammonia Cycling and Emerging Secondary Aerosols from Arable Agriculture: A European and Irish Perspective, Air, 1, 37–54, https://doi.org/10.3390/air1010003, 2022.

Remy, S. and Kaiser, J. W.: Daily global fire radiative power fields estimation from one or two MODIS instruments, Atmos Chem Phys, 14, 13377–13390, https://doi.org/10.5194/acp-14-13377-2014, 2014.

820 Ríos, B. and Raga, G. B.: Spatio-temporal distribution of burned areas by ecoregions in Mexico and Central America, Int J Remote Sens, 39, 949–970, https://doi.org/10.1080/01431161.2017.1392641, 2018.

Saravia, C. and Trachte, K.: Spatiotemporal Analysis of NH3 Emission Sources and Their Relation to Land Use Types in the Eastern German Lowlands, Atmosphere (Basel), 16, 346, https://doi.org/10.3390/atmos16030346, 2025.

Soci, C., Hersbach, H., Simmons, A., Poli, P., Bell, B., Berrisford, P., Horányi, A., Muñoz-Sabater, J., Nicolas, J., Radu, R.,
825 Schepers, D., Villaume, S., Haimberger, L., Woollen, J., Buontempo, C., and Thépaut, J.: The ERA5 global reanalysis from 1940 to 2022, Quarterly Journal of the Royal Meteorological Society, 150, 4014–4048, https://doi.org/10.1002/qj.4803, 2024.

Spencer, N. H.: Squared Euclidean Distances, in: Essentials of Multivariate Data Analysis, 95, 2013.

Sun, K., Tao, L., Miller, D. J., Pan, D., Golston, L. M., Zondlo, M. A., Griffin, R. J., Wallace, H. W., Leong, Y. J., Yang, M. M., Zhang, Y., Mauzerall, D. L., and Zhu, T.: Vehicle Emissions as an Important Urban Ammonia Source in the United States
830 and China, Environ Sci Technol, 51, 2472–2481, https://doi.org/10.1021/acs.est.6b02805, 2017.

Sutton, M. A., Nemitz, E., Erisman, J. W., Beier, C., Bahl, K. B., Cellier, P., de Vries, W., Cotrufo, F., Skiba, U., Di Marco, C., Jones, S., Laville, P., Soussana, J. F., Loubet, B., Twigg, M., Famulari, D., Whitehead, J., Gallagher, M. W., Neftel, A., Flechard, C. R., Herrmann, B., Calanca, P. L., Schjoerring, J. K., Daemmgen, U., Horvath, L., Tang, Y. S., Emmett, B. A., Tietema, A., Peñuelas, J., Kesik, M., Brueggemann, N., Pilegaard, K., Vesala, T., Campbell, C. L., Olesen, J. E., Dragosits,
835 U., Theobald, M. R., Levy, P., Mobbs, D. C., Milne, R., Viovy, N., Vuichard, N., Smith, J. U., Smith, P., Bergamaschi, P., Fowler, D., and Reis, S.: Challenges in quantifying biosphere–atmosphere exchange of nitrogen species, Environmental Pollution, 150, 125–139, https://doi.org/10.1016/j.envpol.2007.04.014, 2007.

Sutton, M. A., Reis, S., Riddick, S. N., Dragosits, U., Nemitz, E., Theobald, M. R., Tang, Y. S., Braban, C. F., Vieno, M., Dore, A. J., Mitchell, R. F., Wanless, S., Daunt, F., Fowler, D., Blackall, T. D., Milford, C., Flechard, C. R., Loubet, B.,
840 Massad, R., Cellier, P., Personne, E., Coheur, P. F., Clarisse, L., Van Damme, M., Ngadi, Y., Clerbaux, C., Skjøth, C. A., Geels, C., Hertel, O., Wichink Kruit, R. J., Pinder, R. W., Bash, J. O., Walker, J. T., Simpson, D., Horváth, L., Misselbrook, T. H., Bleeker, A., Dentener, F., and de Vries, W.: Towards a climate-dependent paradigm of ammonia emission and deposition, Philosophical Transactions of the Royal Society B: Biological Sciences, 368, 20130166, https://doi.org/10.1098/rstb.2013.0166, 2013.

845 Umargono, E., Suseno, J. E., and S. K., V. G.: K-Means Clustering Optimization using the Elbow Method and Early Centroid Determination Based-on Mean and Median, in: Proceedings of the International Conferences on Information System and Technology, 234–240, https://doi.org/10.5220/0009908402340240, 2019.

Vermote, E., Ellicott, E., Dubovik, O., Lapyonok, T., Chin, M., Giglio, L., and Roberts, G. J.: An approach to estimate global biomass burning emissions of organic and black carbon from MODIS fire radiative power, Journal of Geophysical Research: Atmospheres, 114, https://doi.org/10.1029/2008JD011188, 2009.

Wen, Y., Zhang, S., Wu, Y., and Hao, J.: Vehicular ammonia emissions: an underappreciated emission source in densely populated areas, Atmos Chem Phys, 23, 3819–3828, https://doi.org/10.5194/acp-23-3819-2023, 2023.

van der Werf, G. R., Randerson, J. T., Giglio, L., Collatz, G. J., Mu, M., Kasibhatla, P. S., Morton, D. C., DeFries, R. S., Jin, Y., and van Leeuwen, T. T.: Global fire emissions and the contribution of deforestation, savanna, forest, agricultural, and peat fires (1997–2009), Atmos Chem Phys, 10, 11707–11735, https://doi.org/10.5194/acp-10-11707-2010, 2010.

van der Werf, G. R., Randerson, J. T., Giglio, L., van Leeuwen, T. T., Chen, Y., Rogers, B. M., Mu, M., van Marle, M. J. E., Morton, D. C., Collatz, G. J., Yokelson, R. J., and Kasibhatla, P. S.: Global fire emissions estimates during 1997–2016, Earth Syst Sci Data, 9, 697–720, https://doi.org/10.5194/essd-9-697-2017, 2017.

Whitburn, S., Van Damme, M., Clarisse, L., Bauduin, S., Heald, C. L., Hadji-Lazaro, J., Hurtmans, D., Zondlo, M. A., Clerbaux, C., and Coheur, P. -F: A flexible and robust neural network IASI-NH3 retrieval algorithm, Journal of Geophysical Research: Atmospheres, 121, 6581–6599, https://doi.org/10.1002/2016JD024828, 2016a.

Whitburn, S., Van Damme, M., Clarisse, L., Turquety, S., Clerbaux, C., and Coheur, P.-F.: Doubling of annual ammonia emissions from the peat fires in Indonesia during the 2015 El Niño, Geophys Res Lett, 43, 11,007-11,014, https://doi.org/10.1002/2016GL070620, 2016b.

Whitburn, S., Van Damme, M., Clarisse, L., Hurtmans, D., Clerbaux, C., and Coheur, P.-F.: IASI-derived NH3 enhancement ratios relative to CO for the tropical biomass burning regions, Atmos Chem Phys, 17, 12239–12252, https://doi.org/10.5194/acp-17-12239-2017, 2017.

Wolfe, R. E., Nishihama, M., Fleig, A. J., Kuyper, J. A., Roy, D. P., Storey, J. C., and Patt, F. S.: Achieving sub-pixel geolocation accuracy in support of MODIS land science, Remote Sens Environ, 83, 31–49, https://doi.org/10.1016/S0034-4257(02)00085-8, 2002.

Wooster, M., Zhukov, B., and Oertel, D.: Fire radiative energy for quantitative study of biomass burning: derivation from the BIRD experimental satellite and comparison to MODIS fire products, Remote Sens Environ, 86, 83–107, https://doi.org/10.1016/S0034-4257(03)00070-1, 2003.

Wyer, K. E., Kelleghan, D. B., Blanes-Vidal, V., Schauberger, G., and Curran, T. P.: Ammonia emissions from agriculture and their contribution to fine particulate matter: A review of implications for human health, J Environ Manage, 323, 116285, https://doi.org/10.1016/j.jenvman.2022.116285, 2022.

Zhou, C., Zhou, H., Holsen, T. M., Hopke, P. K., Edgerton, E. S., and Schwab, J. J.: Ambient Ammonia Concentrations Across New York State, Journal of Geophysical Research: Atmospheres, 124, 8287–8302, https://doi.org/10.1029/2019JD030380, 2019.

880   Zhou, Y., Zhao, Y., Mao, P., Zhang, Q., Zhang, J., Qiu, L., and Yang, Y.: Development of a high-resolution emission inventory and its evaluation and application through air quality modeling for Jiangsu Province, China, Atmos Chem Phys, 17, 211–233, 2017.